ELSEVIER

Contents lists available at ScienceDirect

# Deep-Sea Research Part II

journal homepage: www.elsevier.com/locate/dsr2





# A data-assimilative modeling investigation of Gulf Stream variability

Shun Mao a, \*, Ruoying He a, John Bane b, Glen Gawarkiewicz c, Robert E. Todd c

- <sup>a</sup> North Carolina State University, USA
- b University of North Carolina, Chapel Hill, USA
- ° Woods Hole Oceanographic Institution, USA

#### ARTICLEINFO

Handling Editor: Dr. K Drinkwater

#### ABSTRACT

An advanced data-assimilative ocean circulation model is used to investigate Gulf Stream (GS) variability during 2017–2018. The modeling system applies a strong-constraint, 4D variational data assimilation algorithm. It assimilates satellitebased sea surface height and sea surface temperature measurements and in situ temperature and salinity profiles. Model skill assessment metrics along with comparisons of GS position and GS's three-dimensional mean kinetic energy with historical observations are applied to validate the data-assimilative model. The resulting time- and space-continuous ocean state estimates are used to diagnose eddy kinetic energy conversion and cross-stream eddy heat and salt fluxes over the two-year study period. The processes leading to kinetic energy conversion are primarily due to GS meanders. Significant inverse energy cascading (EKE-+MKE and EKE-+EPE) can occur during GS-eddy interactions, particularly during onshore intrusions or offshore meanderings of the GS. Throughout the two-year study period, the cross-stream eddy heat and salt fluxes off Cape Hatteras were predominantly positive (onshore). Both GS offshore meandering (occurring 44% of the time and associated with shelf/slope water export) and GS intrusion (occurring 56% of the time) contribute to onshore heat and salt transport. Improved understanding of these processes and dynamics requires strong integration of an advanced observational infrastructure that combines remote sensing, fixed, mobile, and shore-based observing components, and high-resolution data assimilative models.

#### 1. Introduction

Boundaries between subtropical and subpolar oceanic gyres are characterized by confluent western boundary currents and convergence in the adjacent continental shelf and slope waters. This leads to large net export of shelf waters to the open ocean. In the Northwest Atlantic Ocean, such a confluent zone is located offshore of Cape Hatteras, North Carolina, USA, where the compounding effects of the meandering Gulf Stream (GS) and the convergence of adjacent shelf and slope water from the Middle Atlantic Bight (MAB) and South Atlantic Bight (SAB) lead to substantial interactions between the circulation over the shelf and in the deep ocean (Fig. 1).

The GS plays a major role in shaping regional ocean circulation (e.g. Olson et al., 1983; Gula et al., 2015; Zeng and He, 2016). After passing through the Florida Straits, the GS flows over the upper continental slope through the SAB. North of the Straits, the GS passes closest to shore near Cape Hatteras, with the cross-shelf distance from the coast to the GS's shoreward edge being as little as 20 km (12.5 mi). From Cape

Hatteras, the GS detaches from the continental slope and flows generally northeastward into the open ocean. Exchanges between the shelf and open ocean near Cape Hatteras are driven by GS variability, shelf water properties, atmospheric forcing, and local bathymetry (e.g. Savidge and Bane, 2001; Todd, 2020b), and they impact short-term and seasonal variability of water mass composition, pollutant transport, and coastal ecosystem dynamics (Wood et al., 1996; Bignami and Hopkins, 2003; Savidge and Savidge, 2014; Han et al., 2021; Seim et al., 2022).

The variability of the GS and its interaction with shelf currents, the equatorward flow of the slope sea gyre (e.g. Csanady and Hamilton, 1988; Flagg et al., 2006), and the North Atlantic Deep Western Boundary Current (Pickart and Smethie, 1993; Andres et al., 2018) are key topics being investigated as part of the "Processes driving Exchange At Cape Hatteras" (PEACH) research program (Seim et al., 2022). PEACH aims to understand dynamical mechanisms that control exchanges between shelf waters and the open ocean using an integrated observational and modeling approach. New observations collected in 2017–2018 include data from a combination of fixed (moorings), mobile (gliders, ships), and

E-mail address: smao5@ncsu.edu (S. Mao).

Corresponding author.

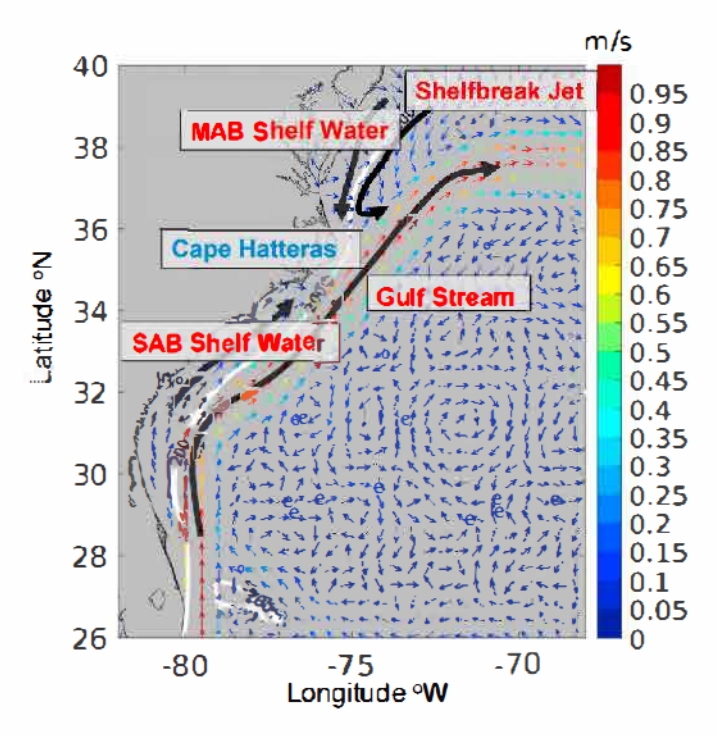


Fig. 1. Schematics show the mean circulation around Cape Hatteras, North Carolina, USA. The vector field represents the 2 year (2017–2018) mean surface velocity derived from the datassimilative model described in this study. Schematic arrows for the MAB shelf water and shelfbreak jet are slightly different from the underlying mean vectors of surface currents due to wind driven processes. Vector color reflects the magnitude of velocity. The 200-m isobath is shown by the white solid line.

shore based (high frequency radar) observing platforms (see Andres et al., 2018; Todd, 2020b; Han et al., 2021; Seim et al., 2022). Data assimilative ocean modeling has also been applied to fill spatial and temporal gaps in observations and to examine processes that cannot be diagnosed directly from the observations.

This paper presents details of the implementation, validation, and application of the data-assimilative modeling system developed for PEACH. Section 2 describes the model set up, the 4D variational data assimilation algorithm, and a suite of observations used for ocean state estimates. An extensive set of model validation is given in Section 3. Model skill assessment metrics, GS position and comparisons of kinetic energy with glider observations are included in this validation section. Detailed analyses using the resulting realistic, continuous ocean state variables are provided in Section 4, first focusing on the modulation of mean kinetic energy (MKE) and eddy kinetic energy (EKE), including barotropic and baroclinic energy conversion, and then on the cross stream (relative to the mean path of GS) eddy fluxes. Section 5 summarizes the results and implications.

## 2. Model and data

# 2.1. Data assimilative model

The Regional Ocean Modeling System (ROMS) was used in this study. ROMS is a terrain following, signa coordinate, primitive equation model developed specifically for regional applications (Haid vogel et al., 2008). Its computational kernel uses high order time stepping and advection schemes and a carefully designed temporal averaging filter to guarantee conservation for tracers and momentum (Shchepetkin and McWilliams, 2005). The model domain (Fig. 2) spans the Northwest Atlantic, Caribbean, and Gulf of Mexico with 7 km (1/15°) horizontal grid spacing and 36 vertical layers. The bathymetry is generated using 1 min gridded GEBCO data and smoothed with a

linear programming procedure (Sikirić et al., 2009) to remove overly large gradients that may lead to unwanted numerical pressure gradient errors in the model (1x0 is kept smaller than 0.3; Beckmann and Haid vogel, 1993). The model uses fourth order centered advection and the generic length scale vertical mixing scheme (Warner et al., 2005). At the domain's only open boundary on the east, the model is configured to conserve volume with a free surface Chapman condition, a Flather condition for the 2 D momentum, and clamped conditions for 3 D mo mentum and tracers (Marchesiello et al., 2001; Powell et al., 2008; Broquet et al., 2009; Moore et al., 2009). Boundary values of ocean state variables are derived from the daily global HYCOM/NCODA product (Metzger et al., 2017). Surface forcing used in the ROMS simulation is derived from the European Center for Medium Range Weather Forecast (ECMWF) reanalysis product, which is available every 3 h at 0.1 25° spatial resolution. Air temperature, surface pressure, humidity, wind speed and direction, short and long-wave radiation, and precipitation from ECMWF are used to compute the ROMS surface momentum and buoyancy forcing with the bulk flux formulation of Fairall et al. (1996). Our data assimilation experiment generated daily snapshots of ocean state variables covering the period from January 2017 through December 2018. The goals were to improve subtidal hydrodynamic simulations during the 2017-2018 PEACH field campaign and to a chieve betterunderstanding of &S variability and its interactions with shelf circulation. Tidal velocities in the Cape Hatteras region are generally weak, as discussed by Andres et al. (2018). While there are tidal ve locities observed over the continental slope and abyss off Cape Hatter as, their impact on the sub tidal circulation and data assimilative modeling is considered negligible. The non-data assimilative forward model simulation was integrated for 3 years from January 1, 2016 to December 31, 2018. The data assimilation experiment focused on a 2 year period from January 1, 2017 to December 31, 2018.

For data assimilation (DA), we applied ROMS's 4-Dimensional Variational Data Assimilation (4D-Var) system, which includes the nonlinear forward model (NLROMS), tangent linear model (TLROMS) and adjoint model (ADROMS). The incremental and strong constraint 4D-var data assimilation algorithm (Courtier et al., 1994) was adopted. Details of the DA methodology were documented in Chen et al. (2014) and Moore et al. (2011a). Interested readers are referred to these studies for more information. For each assimilation window, only the initial condition was modified by the 4D Var procedure; forcing conditions and boundary conditions remained unchanged.

The objective of the 4D Var model is to obtain the most accurate estimation of the ocean state by minimizing a nonlinear cost function. The inner loop of the model consists of a series of linear least squares minimizations, while the outer loop involves regular updates of the tangent linear model at the observation points. In this study, we chose two outer loops and eight inner loops, given that multiple loops are considered advantageous since the convergence of the cost function to its minimum can be accelerated by secondlevel preconditioning predicted on the previous outer loop (Moore et al., 2011b). A three day assimilation window was chosen because a short window maintains the tangent linear approximation in a nonlinear GS regime and controls model trajectories more effectively (Powell et al., 2008; Broquet et al., 2009; Chen et al., 2014). In addition, a one day overlap between assimilation windows was applied as was done in Powell et al.: (2008) and Chen et al. (2014) to support smooth transitions between adjacent assimilation windows.

## 2.2. Observational data

# 2.2.1. Sea surface height anomaly

The model assimilates level 4 sea surface height anomaly (SSHA) data processed and distributed by the Copernicus Marine and Environment Monitoring Service. The gridded SSHA data we utilized in our study corresponds to the product ID "SEALEVEL\_GLOPHY\_L4\_REP\_OBSERVATIONSO08\_047", obtained from the European

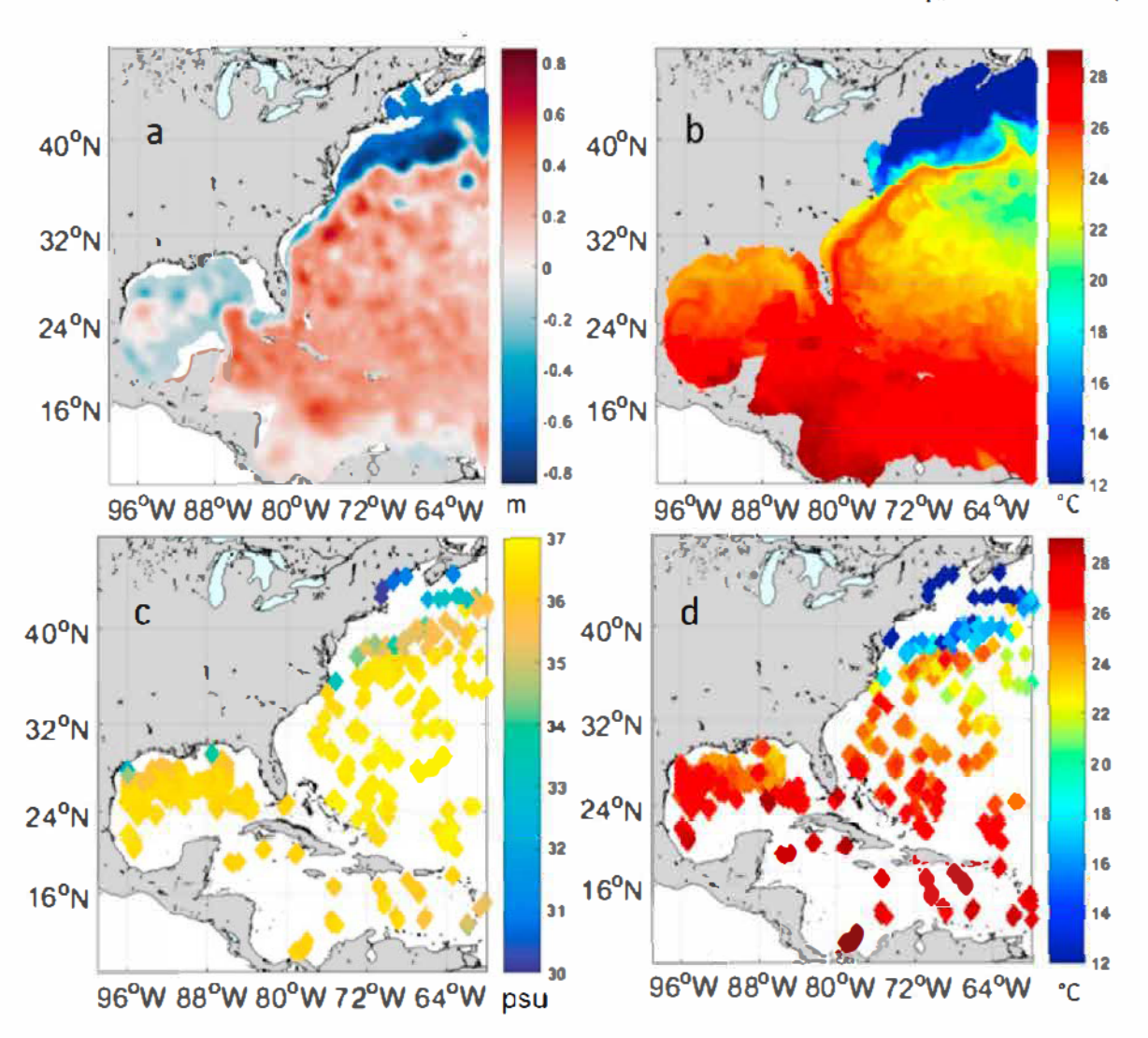


Fig. 2. Example of observations showing (a) sea surface height (SS H) on May 1, 2017 and (b) sea surface temperature (SST) on May 1, 2017. Also show n are surface observations of (c) in situ salinity and (d) temperature profiles for all of May 2017.

Copernicus Marine Environment Monitoring Service (CMEMS)". These data cover the period from 2017 through 2018 and combines data from multiple satellites active during this period, namely Jason2, CryoSat-2, SARAL AltiKa, Jason 3, and Sentinel 3. This product is available on a daily basis with a horizontal resolution of 1/4°. Before the 4D Var assimilation, the anomalies were converted to sea surface height (Fig. 2a) by adding the 20 year mean sea level from HYCOM. Doing so allows for consistency between the sea level data being assimilated in the model's interior and the sea level open boundary conditions from HYCOM. As in Chen et at. (2014), we excluded sea surface height data located shoreward of the 200m isobath due to the uncertainty of the satellite altimeter product in the coastal ocean.

The GeoPolar Blended Sea Surface Temperature (SST) data (Fig. 2b) developed by the NOAA CoastWatch program is a 5 kmresolution, cloud free, optimally interpolated SST dataset. It ingests SST observation from GOES, AVHER, and MOD16 satellites and is available daily from 2002 to the present.

## 2.2.2. Subsurface temperature and salinity

Quality controlled hydrographic data (EN4) were processed by the European Union ENSEMELES project. These data are archived by the UK Met Office (Ingleby and Huddleston, 2007; Good et al., 2013), providing valuable subsurface hydrographic observations. Within our model domain, this temperature and salinity dataset (Fig. 2c and d) contains in situ observations archived by the World Ocean Database, the Global

Temperature Salinity Profile Program, and the USGODAE Argo Global Data Assembly Centers. Ocean temperature and salinity profiles from Spray underwater gliders sampling within the GS (Heiderich and Todd, 2020) and over the upper continental slope and outer continental shelf near Cape Hatteras for PEACH (see Todd, 2020a,b) provided important water mass information to our data assimilative model.

## 2.2.3. "Super observations" and observational error

As in Chen et al. (2014), we bin averaged surface and subsurface observations into "super observations" to ensure that no more than one measurement of a particular state variable was included in a particular model grid at any time step.

The observational error covariance matrix R was chosen to be the larger of the variance of the measurement error and error of representativeness. The error of representativeness was calculated as the standard deviation of the observations within each "super observation." The measurement error variances were chosen independently for different data sources (Broquet et al., 2009; Chen et al., 2014). Following previous researchers' parameter choices, we chose measurement errors of 0.02m and 0.4 °C (Powell et al., 2008) for SSHA and SST, respectively. For in situ temperature and salinity profiles, measurement errors of 0.1 °C and 0.1 psµ were used (Chen et al., 2014). We choose these measurement errors that are larger than the instrumental errors for each platform to avoid overfitting of the observations.

#### 3. Data-assimilative model performance assessment

Here we first confirm that the 4D-Var data assimilation produced a numerical simulation that better agrees with assimilated observations than does the forward (non-data-assimilating) simulation (section 3.1). We calculate a variety of widely used metrics of model-data mismatch for this purpose. In section 3.2 we compare GS position from altimetry data with that from our 4D-Var data assimilation results. In section 3.3, model shows decent GS velocity structure and transport, despite not assimilating velocity. Finally, in section 3.4, we compare mean kinetic energy and eddy kinetic energy from glider-based observations with that from DA model results.

## 3.1. Reduction of model errors

Time series of the domain-averaged SSH root mean squared error (RMSE) provide a direct way to evaluate the DA model performance (Fig. 3). For both forward-modeled (no DA) and DA-modeled SSH fields, RMSE is computed daily as

**RMSE** 
$$\left(\frac{1}{N}\sum_{i=1}^{N}\left(y_{i}^{m}-y_{i}^{n}\right)^{2}\right)^{1/2}$$
 (1)

where N is the number of observations,  $y_i^m$  is the modeled state variable, and  $y_i^o$  is the observed state variable. Without DA, the forward model SSH RMSE ranges from 0.12 to 0.28 m. DA SSH RMSE is much lower, ranging from 0.06 to 0.15 m with a mean value of 0.08 m. Except for brief amplifications during September–October in 2017 and 2018 when several energetic hurricanes transited the model domain, the DA SSH RMSE mostly stays below 0.12 m, showing that the DA model's ability in simulating the dynamic SSH topography is better than that of the model without DA

The bias error represents the overall discrepancy between model output and observations and identifies whether the model systematically over- or underestimates a variable.

$$Biaserror = \frac{1}{N} \sum_{i=1}^{N} (y_i^m - y_i^\rho)$$
 (2)

We computed the bias error for the simulated subsurface temperature and salinity from both the forward and DA models. The vertical distribution of horizontally and temporally averaged subsurface temperature and salinity biases shows that DA helps to decrease largest temperature bias from 0.5 to 0.1 °C, and largest salinity bias from 0.5 to -0.02 ps $\mu$  in the upper 200 m (Fig. 4a and b). Temperature biases are largest near 80 m in the thermocline, where they are reduced from 0.6 °C to 0.2 °C by DA. Near the surface, however, the temperature bias changes sign and has nearly the same magnitude following DA (Fig. 4a). Near-surface salinity bias is reduced from 0.6 to nearly zero and subsurface salinity bias is reduced at most other depths (Fig. 4b). Daily time series of domain-mean temperature and salinity bias (Fig. 4c and d) also indicates that the DA model, after assimilating temperature and salinity observations, has substantially reduced bias compared to the forward model.

Following Stow et al. (2009), we applied five additional skill assessments to the forward model and DA model solutions for SSH, SST, subsurface temperature, and subsurface salinity (Table 1). These assessment metrics are the RMSE (Eq. (1)), correlation coefficient (Eq. (3)), reliability index (Eq. (4)), average absolute error (Eq. (5)), and modeling efficiency (Eq. (6)). Their formulae are:

$$CorrelationCoeffice int = \frac{\sum_{i=1}^{N} (y_i^o - y_i^o) (y_i^m - y_i^m)}{\sqrt{\sum_{i=1}^{N} (y_i^o - y_i^o)^2} \sum_{i=1}^{N} (y_i^m - y_i^m)^2}$$
(3)

ReliabilityIndex = 
$$exp \sqrt{\frac{1}{n} \sum_{i=1}^{N} \left(log \frac{y_i^o}{y_i^m}\right)^2}$$
 (4)

$$\sum_{i=1}^{N} |y_i^n - y_i^o|$$
Average Absolute Error  $-\frac{i-1}{n}$  (5)

Modeling efficiency = 
$$\frac{\left(\sum_{i=1}^{N} (y_i^o - \overline{y^o})^2 - \sum_{i=1}^{N} (y_i^m - y_i^o)^2\right)}{\sum_{i=1}^{N} (y_i^o - \overline{y^o})^2}$$
 (6)

The correlation coefficient measures how well the predicted and observed values vary together. Ideally this should be close to 1. The reliability index (RI) indicates the average factor by which model prediction differs from observation. Ideal RI should also be close to 1. The average absolute error measures the size of discrepancies between predictions and observations. A value near 0 indicates a close match. Finally, the modeling efficiency indicates how good the model prediction is relative to the average of the observations. A value near 1

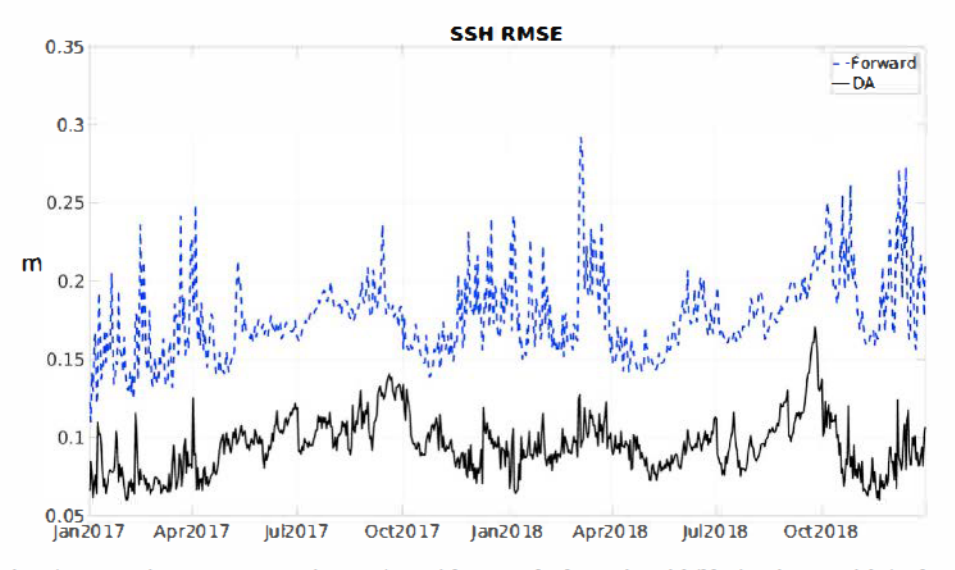


Fig. 3. Comparison of the domain-averaged root mean squared errors (RMSE) between the forward model (blue) and DA model-simulated (black) SSH fields from January 2017 through December 2018.

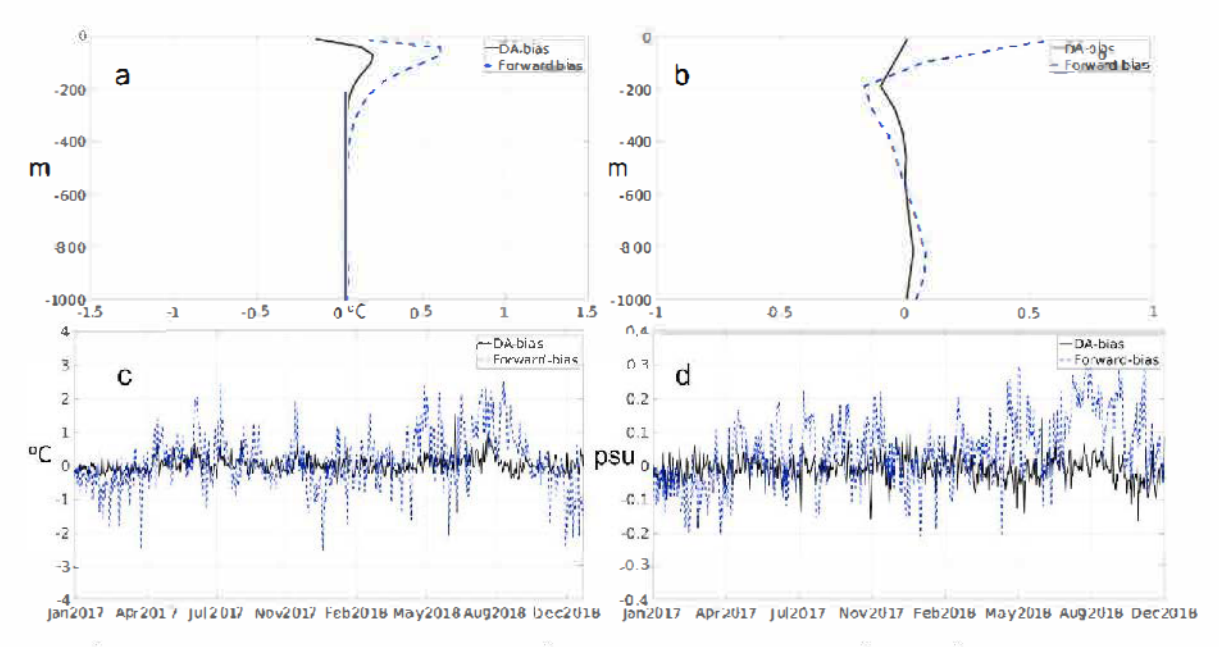


Fig. 4. Vertical distribution of horizontally and temporally averaged (a) subsurface temperature and (b) salinity bias errors between the forward and DA models from January 2017 to December 2018. Also shown are the time series of domain averaged (c) temperature and (d) salinity bias errors.

Table 1
Statistical scores of the forward model and DA model in reproducing sea surface height (SSH), sea surface temperature (SST), subsurface temperature, and salinity in January 2017-December 2018.

Models	SSH		SST		Temperature		Salirity	
	Forward model	DA model	Forward model	DA model	Forward model	DA model	Forward model	DA model
Correl ation Coefficient	0.80	0.85	0.64	0.99	0.93	0.98	0.82	0.98
Root mean squared error	0.18(m)	0.09(m)	4:25 (°C)	0,46 (°C)	2.40 (°C)	1.38 (°C)	0.79 (psu)	0.31 (psu)
Reliability Index	0.91	1.02	1.30	1.03	1.22	1.12	1.03	1.01
Average Absolute Error	0.13(m)	0.1(m)	3.08 (°C)	0.31 (℃)	1.74 (°C)	0.86 (°C)	0.57 (psu)	0.18 (psu)
Modeling Efficiency	0.56	0.70	0.25	0.99	0.86	0.96	0.60	0.96

indicates a close agreement between model predictions and observations. Both the correlations and the model efficiency scores are computed by removing constant mean values from the observed and modeled data, so these metrics primarily reflect model observation agreement at the largest spatial scales of variability.

We compute each of these metrics of model skill for both the forward and 4D Var model runs (Table 1). The 4D Var assimilation procedure leads to correlation coefficients increasing from 0.8 to 0.85 for SSH from 0.64 to 0.99 for SST. For the subsurface properties, DA improves the correlation coefficient of subsurface temperature (subsurface salinity) from 0.93 (0.82) to 0.98 (0.98). The DA procedure results in reductions of RMSE of 50% for SSH, 76% for SST, 43% for subsurface temperature, and 61% for subsurface salinity. For the reliability indices, the DA model results bring this assessment closer to 1 for the SSH and subsurface salinity and reduces the reliability indices of the forward model for SST and subsurface temperature by 21% and 8% respectively. The average absolute errors of the DA model for SSH, SST, subsurface temperature, and subsurface salinity decreased by 0.03 m, 2.77 °C, 0.88 °C, and 0.39 compared with the forward model. DA model also helps to improve modeling efficiency scores of surface products from 0.56 to 0.70 for the SSH and from 0.25 to 0.99 for the SST. Modeling efficiency scores of the forward model for subsurface temperature and subsurface salinity are 0.86 and 0.60, respectively. In contrast, the DA model increases both these values to 0.96. Overall, even though forward model results have good correlation coefficients and modeling efficiency scores for SSH and SST, 4D-Var data assimilation results in better skill overall in generating a highly realistic ocean reanalysis, particularly for the subsurface ocean state variables.

# 3.2. Gulf stream position

Several approaches have been used in earlier studies to identify the position of the GSe 1) the maximum SSH gradient (e.g. Qiu and Chen, 2006; Zeng and He, 2016), which represents the core rather than the edge of the GS; 2) a constant contour (e.g. 25 cm) of the gridded dynamic topography measured by satellite altimeters (e.g. Lillibridge and Mariano, 2013; Andres et al., 2020); and 3) the location of a particular isotherm at a particular depth (e.g. the 12 °C isotherm at 400 m (Halkin and Rossby, 1985) or the 15 °C isotherm at 200 m (Fuglister and Voorhis, 1965)). Our discussion here focuses on comparing the first two approaches, which are based on ocean surface conditions so can be directly compared between modeled output and satellite observations. We are interested in the differences between these two methods because they are based on dynamic SSH topography.

For this study, we focus on the GS position near Cape Hatteras and the GS extension region between 68°W and 78°W. The two year mean GS positions identified by modeled maximum gradient method and by the satellite 25 cm contour method generally align with each other (Fig. 5). However, notable differences in temporal variability are noted around Cape Hatteras: GS positions defined by the maximum gradient has a wider envelope (Fig. 6) near Cape Hatteras and west of 70°W. Daily GS positions from the modeled maximum gradient method (Fig. 6a) and the modeled 25 cm contour method (Fig. 6b) show a broader GS position spread than that from the satellite 25 cm contour (Fig. 6c), especially west of 71°W. This may be because the satellite SSH field, being a blended product with an effective temporal resolution of ~10 days (the altimetry repeat cycle), underrepresents the temporal

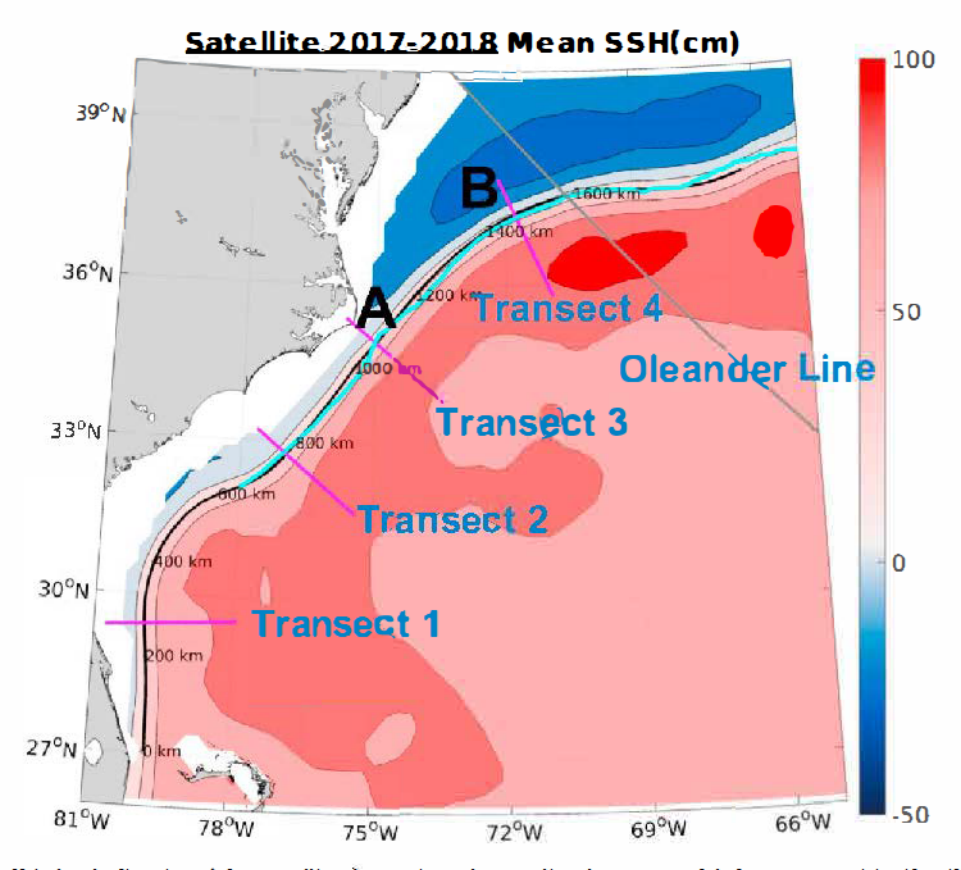


Fig. 5. Two year mean SSH (color shading, in cm) from satellite observations. The cyan line shows DA modeled GS mean position identified by the maximum SSH gradient, and the black line represents the GS mean position identified by the 25-cm contour of satellite-observed SSH. A and B mark points used for analyses. Also shown are the locations of four cross-shelf transects (magenta) and the Oleander line (gray).

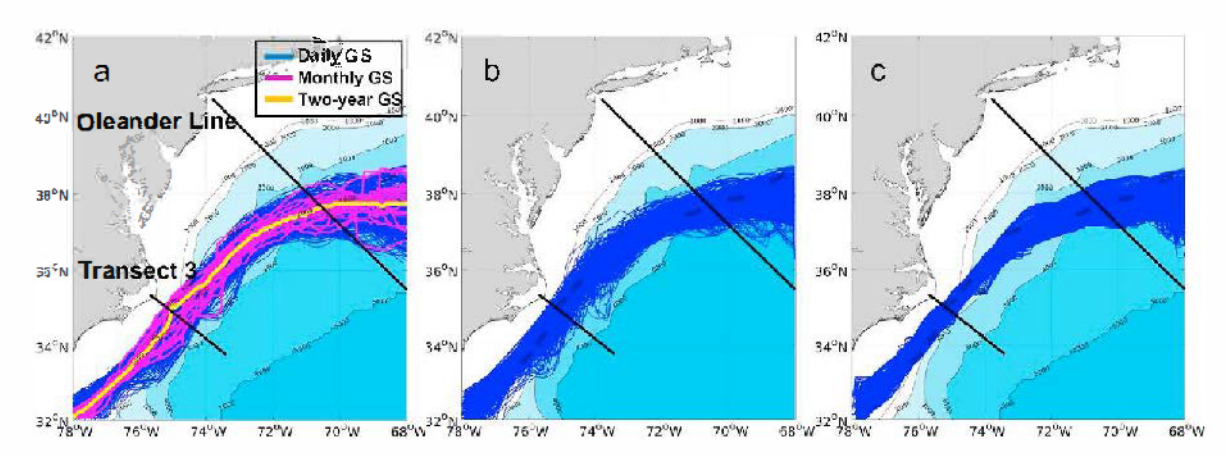


Fig. 6. Daily GS position (blue lines) during January 2012December 2018 as defined by (a) the maximum gradient of DA modeled SSH; (b) the 25-cm contour of DA-modeled SSH (adjusted to the reference level of satellite SSH); and (c) the 25-cm contour of satellite SSH. In panel a), the magentalines denote the monthly mean GS positions from the DA model, and the yellow line denotes the two-year mean GS positions from the DA model A so shown in thick blacklines in each panel are the locations of the Oleander line and transect 3, where the GS cross-shelf distances were calculated. Ocean bathymetry is indicated in light blue cobr shading.

variability of the GS. It is also possible that  $\pi$  nodel overestimates the temporal variability.

We expanded the comparison by examining the GS offshore distance from January 2017 through December 2018 along the Oleander line (e. g. Flagg et al., 1998; Rossby and Benway, 2000; Andres et al., 2020) and transect 3 (Fig. 6). During this two year period, the GS offshore positions along the Oleander line (a bout 1200 lun between Port Elizabeth, New Jersey, and Hamilton, Bermuda.) identified by the two methods (Fig. 7a) show general agreement... The correlation coefficient between the GS offshore distance identified by modeled maximum gradient (by modeled

contoin) and that identified by satellite altimetry contoin is 0.85 (0.92). The GS meandered between 350 km and 500 km offshore along the Oleander line. Detailed examinations of the surface fields from both model simulations and satellite observations show that a GS offshore meander in January 2018 and a GS onshore intrusion in February 2018 contributed to the up to 150 km shift of GS location along the Oleander line. Applying the 25 cm contour on the satellite gridded SSH fields is indeed a robust way to identify the GS positions along this transect, as has been shown by earlier studies (e.g. Andres et al., 2020).

In contrast, larger discrepancies in GS position between the model

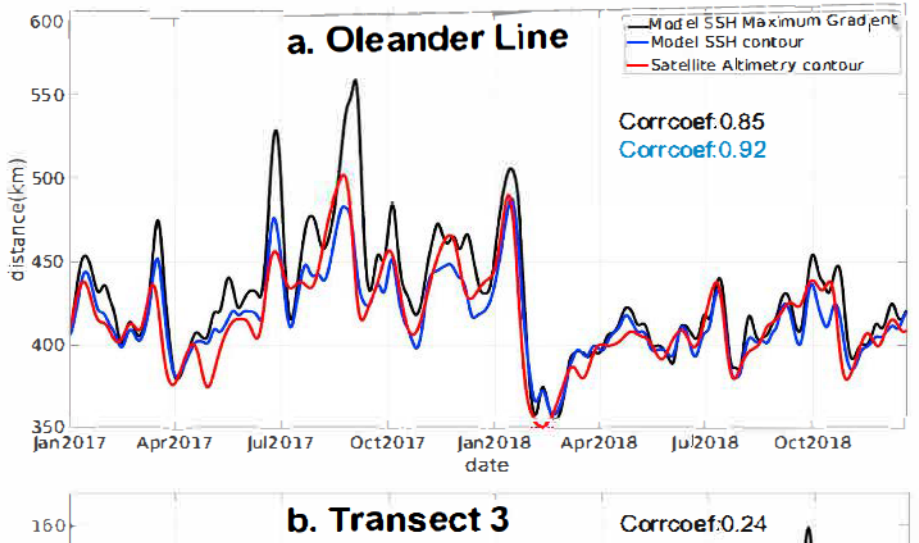
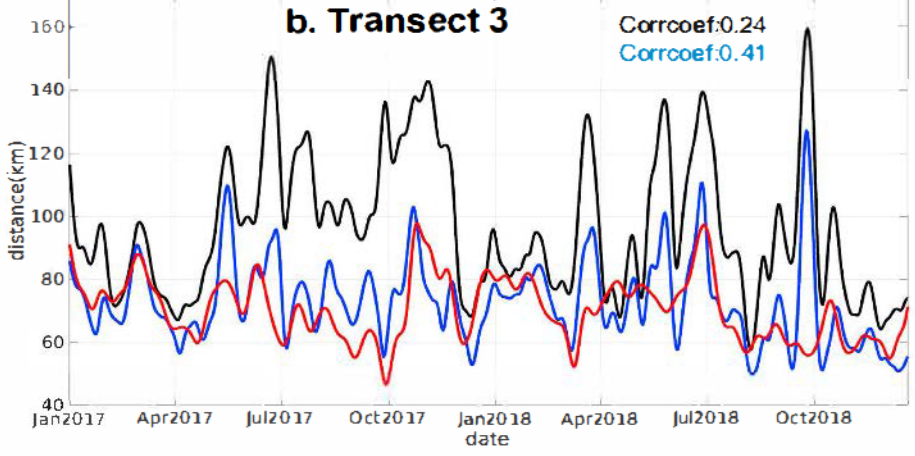


Fig. 7. GS offshore distance identified by DA-modeled maximum SSH gradient (black), DA-modeled 25-cm contour (adjusted to the reference level of satellite altimetry, blue), and satellite altimetry SSH 25-cm contour (red) at a) the Oleander line and b) Transect 3 near Cape Hatteras. See Fig. 5 for transect locations. The values of temporal correlation coefficients between the GS off shore distance identified by DA-modeled maximum SSH gradient (by DA-modeled 25-cm contour) and by the satellite altimetry SSH 25-cm contour are provided for each transect and shown in black (blue).



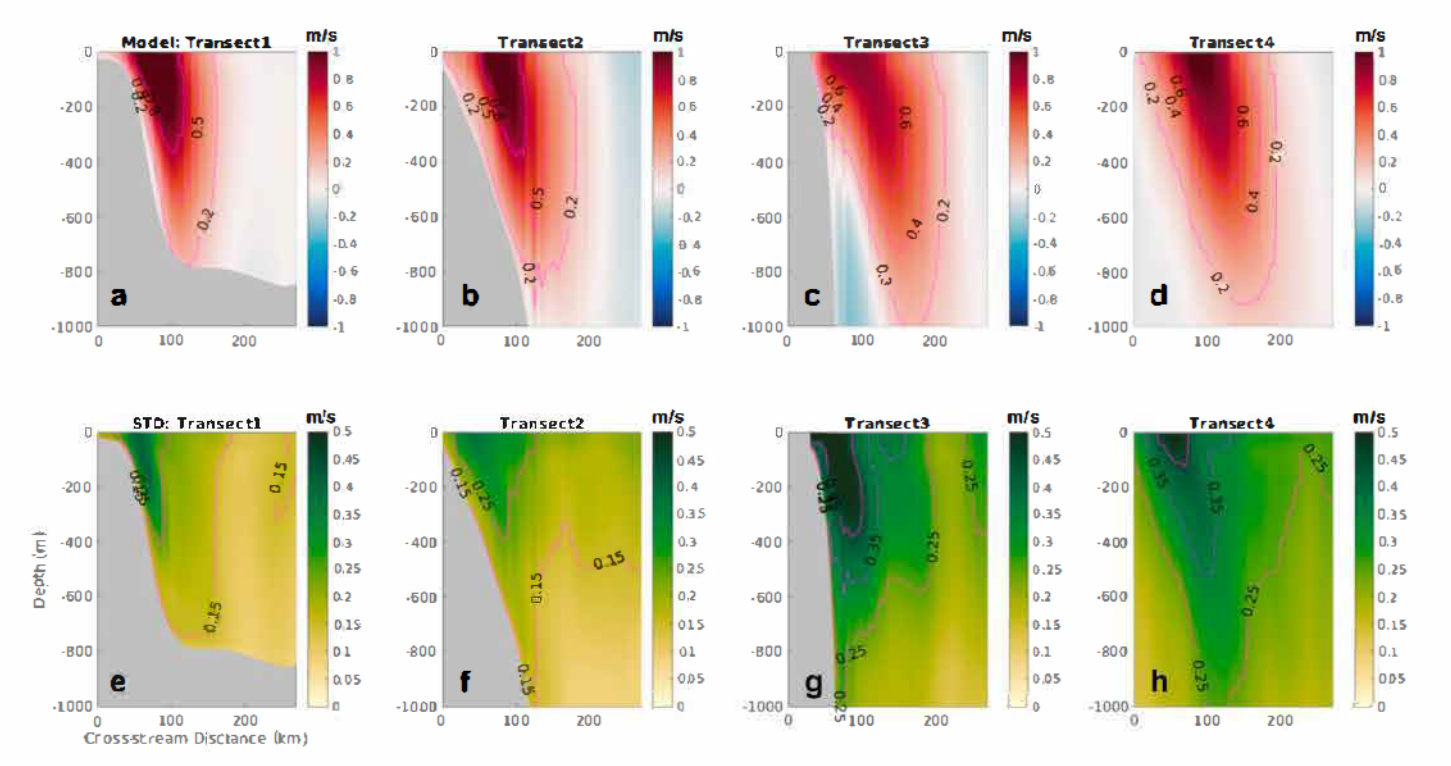


Fig. 8. Modeled GS velocity structure along the four transects (magenta lines in Fig. 5), with contours shown. Upper panels show two-year mean velocity fields (Positive velocities represent poleward flow and negative velocities represent equatorward flow). Lower panels show their standard deviation.

and satellite methods are seen along Transect 3 (Fig. 7b), as demonstrated by lower temporal correlation coefficients between pairs (r = 0.24, 0.41). This makes tracking the GS off Cape Hatteras a challenging task. Here, the GS position identified by the modeled maximum gradient was generally 10–40 km farther offshore than the positions identified by the modeled 25-cm contour. The latter is 10–20 km farther offshore than that identified by the satellite 25-cm contour (Fig. 7b). These results suggest that the position of GS core identified by the maximum gradient method cannot be accurately represented by the 25-cm SSH contour off Cape Hatteras.

## 3.3. Velocity and transport of GS

Modeled subsurface velocity (Fig. 8) was sampled along four transects (magenta lines in Fig. 5). As in Todd (2021b), these cross-shelf transects are perpendicular to the mean SSH contour. Mean velocity components at all four transects display a strong, compact GS jet. The core of the GS (speed >0.5 m/s) is located in the upper 600 m. At transects 3 and 4, the flow field experiences large variability associated with meanders, as shown by the >0.25 m/s standard deviation contours that are over 100 km wide and 1000 m deep at transects 3 and 4.

The mean GS transport measured by the Florida Strait cable from 2017 to 2018evas 32.1  $\pm$  3.0 Sv, while the model's mean transport was 29.6  $\pm$ 2.8 Sv. The underestimation of the GS transport in the model could potentially be attributed to the relatively coarse horizontal resolution utilized, considering the narrow width (~80 km) of Florida Strait. We also estimate the volume transport of the GS from the time-averaged velocity field for the two-year study period 2017-2018 at each cross-stream transect by integrating all poleward mean flow between the surface and 1000 m. The modeled upper-1000-m transport increased from 40.50 Sv at transect 1-52.08 Sv at transect 2 and to 58.51 Sv at transect 3 off Cape Hatteras. The modeled transport at transect 3 is 1-4 Sv larger than the observed upper-1000-m transport at Cape Hatteras (57.3 Sv for the upper bound and 54.5 Sv for the lower bound from Heiderich and Todd, 2020). Overall, our model is able to capture the observed along-stream increase of GS volume transport as waters are entrained from the open-ocean and the shelf and slope (e.g. Heiderich and Todd, 2020; Andres et al., 2020), despite not assimilating velocity observations.

#### 3.4. Kinetic energy of the GS

The GS is a large oceanic reservoir of kinetic energy in the North Atlantic. Its energy is composed of both mean kinetic energy (MKE) and eddy kinetic energy (EKE). Using kinetic energy as metrics to validate a model is a novel and stringent task given that velocity field needs to be highly accurate, and velocity is not assimilated into our model. How MKE and EKE are partitioned in various parts of the GS has been a long-standing research question (Richardson, 1983a, 1983b; Rypina et al., 2012; Todd, 2021b). Ocean velocity (u,v) can be divided into time-averaged and fluctuating parts: (u,v) = ((u),(v)) + (u',v')e Mean and eddy kinetic energy per unit mass can then be represented as:

$$MKE = \frac{1}{2} \left( \langle u \rangle^2 - \langle v \rangle^2 \right)$$
 (7)

$$EKE = \frac{1}{2} \begin{pmatrix} u^2 & v^2 \end{pmatrix}$$
 (8)

## 3.4.1. Sw face MKE and EKE distribution

Here we compare estimates of MKE and EKE from the model with three-dimensional estimates from glider measurements of velocity and with estimates computed from satellite based SSH (Fig. 9). Satellite-derived KEs were generated using 0.25° × 0.25° satellite gridded SSH fields and their associated geostrophic velocity, whereas the glider-based estimates of MKE and EKE were produced by combining in situ velocity measurements from 31 glider deployments during July 2015–June 2020 (see Todd, 2021b).

All three MKE estimates show very similar patterns and magnitude at the surface, with a maximum value close to  $1 \text{ m}^2/\text{s}^2$  occurring between 27°N and 30°N (Fig. 9, upper panels). In contrast, a noticeable difference in EKE is seen among the three estimates, especially in the SAB (Fig. 9, lower panels). Both the DA model and glider observations show a local EKE maximum near the Charleston Bump at 32eN, where GS offshore deflection and instability often occur (Brooks and Bane, 1978; Bane and Dewar, 1988; Bane et al., 2001; Zeng and He, 2016). However, this local high EKE feature is not captured in the satellite observations due to the coarse spacing of satellite ground tracks ( $\sim$ 10 km). The largest values of EKE (up to 0.5  $\text{m}^2/\text{s}^2$ ) are found downstream of Cape Hatteras in the GS extension area,

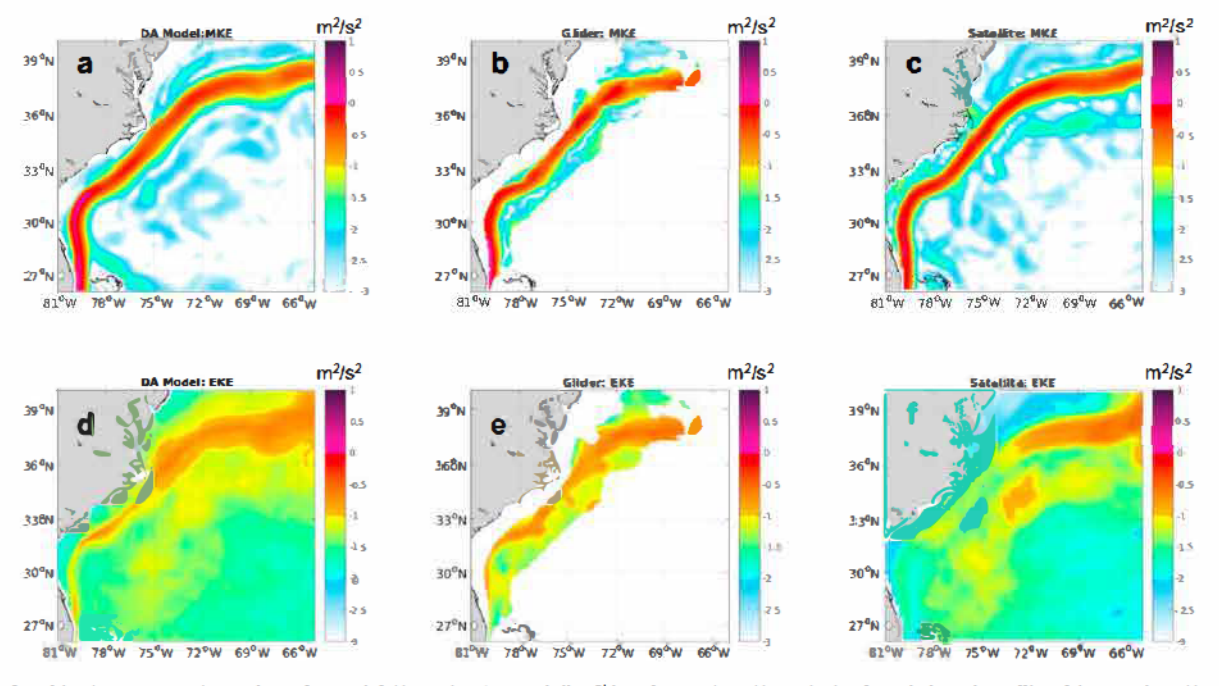


Fig. 9. Surface kinetic energy estimate from the model (2017–2018; a and d), glider observations (2015-2020; beand e), and satellite altimetry data (2017–2018; c and f) Upper (lower) panels show mean kinetic energy (eddy kinetic energy) in log<sub>10</sub> transformed values.

where the GS has large meanders (Rossby, 1987).

## 3.4.2. Subsurfuce MKE and EKE along the Gulf Scream path

Satellite observations can only depict ocean conditions on the surface, so we turn to the DA model and glider data for subsurface kinetic energy structures. Both model output and glider observations of MKE vertical structure along the four cross-shelf transects (Fig. 10) indicate that MKE magnitude decreases with increasing depth, and the local maximum shifts offshore with increasing depth. There are two features that differentiate the model results from glider observations: 1) modeled MKE local maxima on transects 1 and 2 are slightly larger and deeper than those from glider observations, and 2) the modeled local MCE maximum along transect 4 is farther offshore than the glider-based estimate. Different resolutions between model and glider observations may have contributed to these differences. The model's horizontal and vertical resolutions may not be sufficient to resolve the density gradients and their companion strong velocity shears as observed by the glider. Nevertheless, we see a general consistency in the MKE patterns and magnitudes between the glider observation and DA model along all four transects.

A similar comparison was made for subsurface EKE fields between the model and glider observations (Fig. 11). Both modeled and observed EKEs show a gradual increase in EKE magnitude as the GS moves downstream from transect 1 to transect 4. The general locations of EKE maxima are also consistent between the modeled and observed products along all four transects. The model underestimates EKE magnitude and tends to distribute energy deeper in the water column (especially at transect 4) than its observational counterpart. The reason that GS in our model reaches deeper than observations is due to the relatively coarser vertical resolution. Likewise, energetic eddies (especially those of small scale) that were sampled by glider surveys cannot be well resolved by a 7-km resolution ocean model, even with assistance from advanced data assimilation.

#### 4. Analyses

We use our resulting time- and space-continuous ocean state estimates to diagnose processes of kinetic energy conversion in section 4.1 and cross-stream eddy heat and salt fluxes in section 4.2 over the two-year study period. These analyses are not practical if using observations directly. Since the eddy heat and salt fluxes depend not only on cross-stream velocity, but also on water properties across transects, it is important to address the topics of kinetic energy conversions and eddy heat/salt flux separately.

#### 4.1. Modulation of GS MKE and EKE

To understand how MKE and EKE are modulated temporally and spatially, especially between transects 3 and 4 where both glider observations and the model show increases in MKE and EKE, we next quantify several relevant energy conversion terms in the EKE governing equation, as has been done in several previous studies (Masina et al., 1999; Jouanno et al., 2012). These are barotropic instability (BT), baroclinic instability (BC), and advection (ADV):

$$BT = -\left[u^{x}u^{x}\frac{\partial \acute{U}}{\partial x} + u^{x}v^{x}\left(\frac{\partial \acute{U}}{\partial y} + \frac{\partial \acute{V}}{\partial x}\right) + v^{x}v^{x}\frac{\partial \acute{V}}{\partial y}\right] \tag{9}$$

$$BC = \frac{g}{\rho_0} \rho^t w^t \tag{10}$$

$$ADV_{-}\left(\overrightarrow{U} + \overrightarrow{u^{t}}\right) \bullet \nabla EKE \tag{11}$$

where  $\dot{U}$  and  $\dot{V}$  are the horizontal components of the 30-day low-pass filtered velocity,  $u^{\tau}$  and  $v^{\tau}$  are the perturbation velocity components with respect to  $\dot{U}$  and  $\dot{V}$ ;  $w^{\tau}$  is the perturbation of vertical velocity; and  $\rho^{\tau}$  is the density perturbation. Given the GS variations downstream of the Cape Hatteras typically occur on a time scale ranging from weeks to

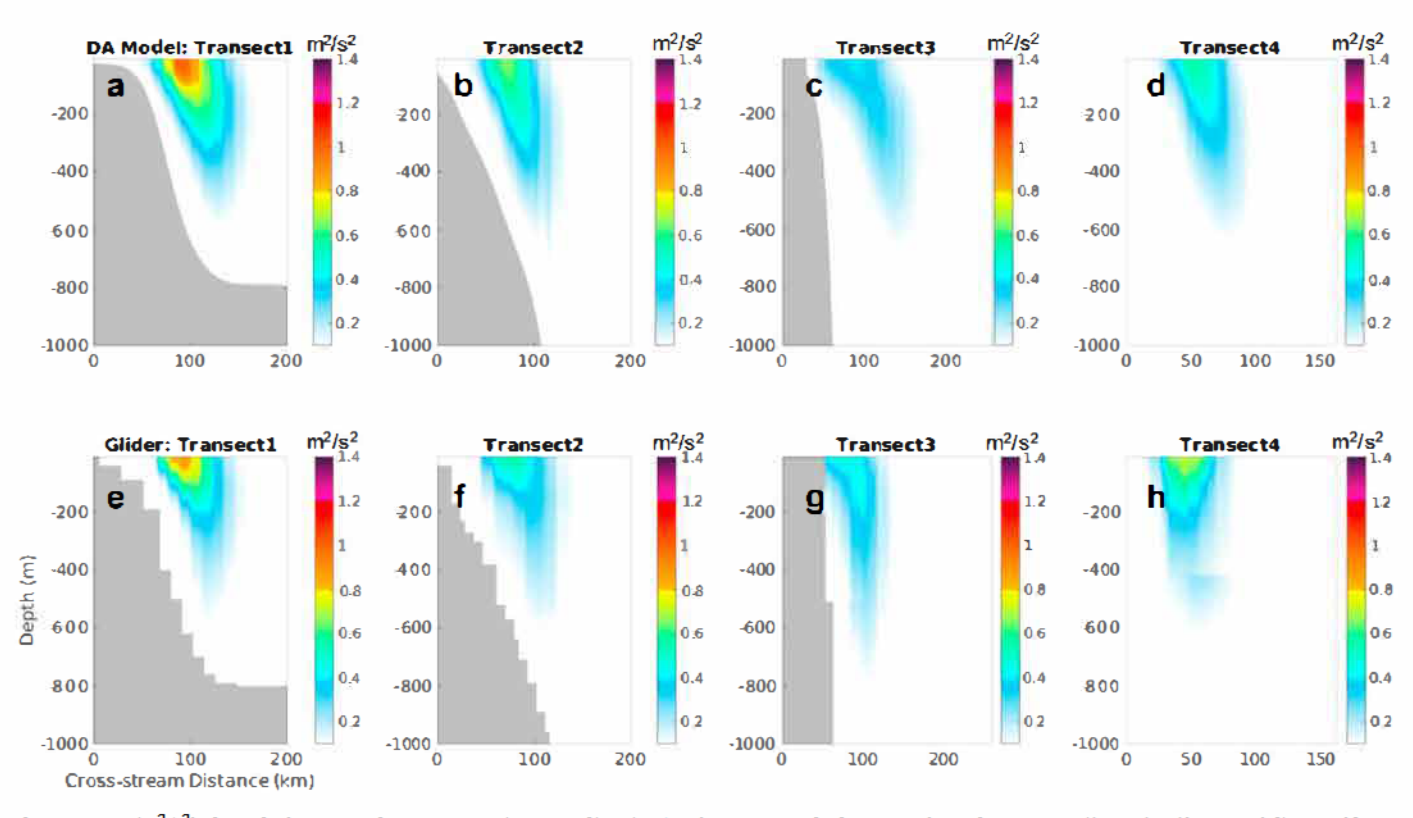


Fig. 10. MKE (m<sup>2</sup>/s<sup>2</sup>) along the four crossshore transects (magenta lines in Fig. 5). Upper panels show MKE from the two-year (2017–2018) DA modeling, and lower panels show MKE from glider observations during 2015-2020 (Todd, 2021a,b; Todd and Owens, 2016).

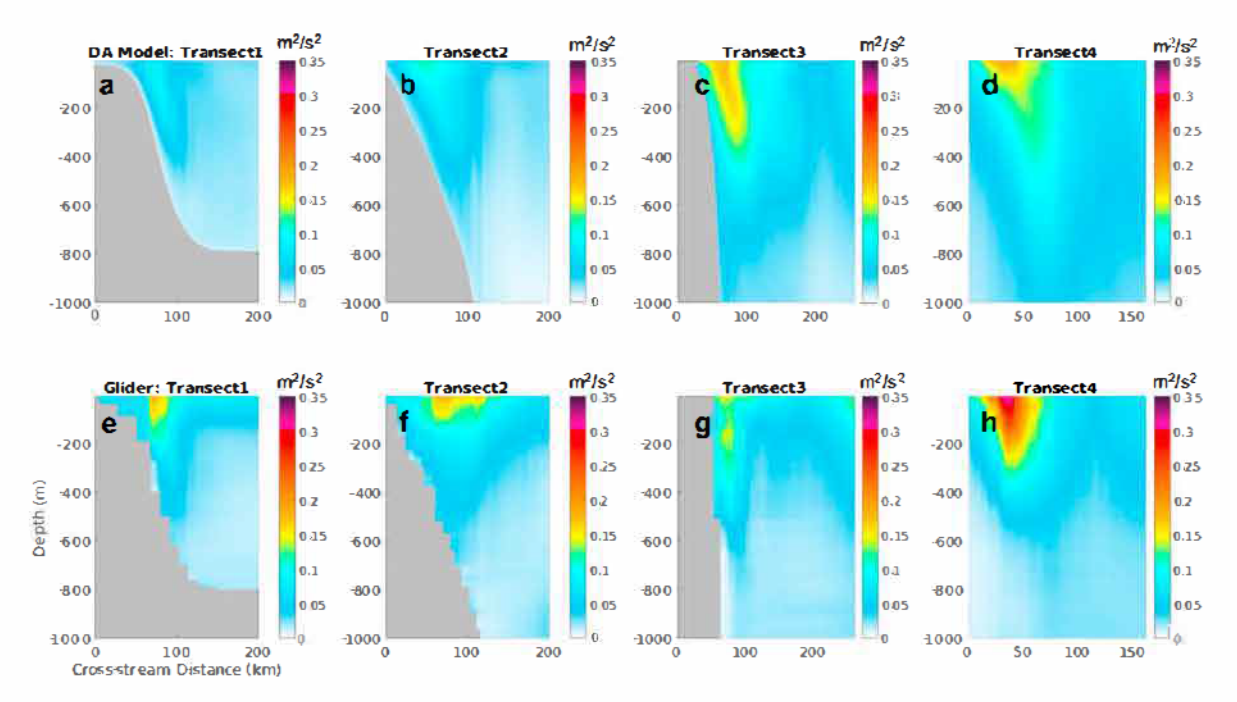


Fig. 11. EKE along the four crossshore transects (magenta lines in Fig. 5). Upper panels show EKE from the two-year (2017-2018) DA modeling, and lower panels show EKE from glider observations during 2015-2020 (Todd, 2021a,b; Todd and Owens, 2016).

months (e.g. Tracey and Watts, 1986), we applied a 30-day low-pass filter to produce a low-frequency circulation  $(\vec{U})$ , from which eddy flow fields  $(\vec{u^t})$  can be characterized and quantified. Different from the definitions in Eq. (7) and Eq. (8), MKE in this section is defined as  $\frac{1}{2}(\vec{U}^2 + \vec{V}^2)$  and EKE is defined a  $\frac{1}{2}(\vec{U}^2 + \vec{V}^2)$ .

The energy production term BT is related to barotropic instability and describes the MKE $\rightarrow$ EKE conversion through eddy momentum flux BC is due to baroclinic instability and represents the energy transfer from eddy potential energy [EPE:  $(g\rho^*)^2/(2\rho_0^2N^2)$  to EKE through ver-

tical eddy density flux. ADV represents the advection of EKE by horizontal currents. For our analysis, we further integrated these terms along transects 3 and 4 over the upper 200 m. ADV is generally one order of magnitude smaller than both BT and BC, and thus will not be discussed in the following section.

Over the two-year period, the sectional mean MKE (EKE) is about 31% (64%) more at transect 4 than transect 3 (Fig. 12 a, b). This is consistent with findings from Figs. 10 and 11, suggesting the GS is becoming stronger, but also more prone to instability, as it passes Cape Hatteras. MKE variations at transect 3 and transect 4 are poorly

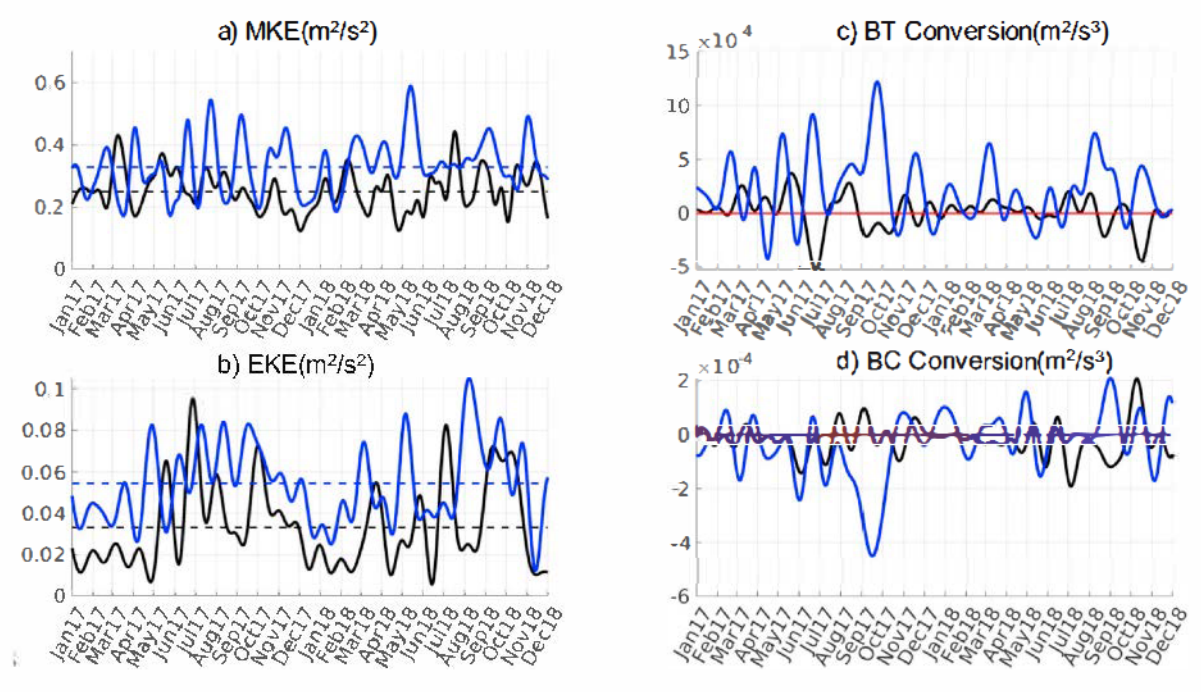


Fig. 12. 30-day low-pass filtered time series of a) sectional mean MKE; b) sectional mean EKE; c) sectional mean barotropic conversion; d) sectional mean baroclinic conversion. Black (blue) colored lines represent results along transect 3 (transect 4). Dashed lines in a) and b) indicate their corresponding MKE and EKE mean values. Red lines indicate zero value. Note the change of scales in all subplots.

correlated. Correlation r only eeaches a maximum value of  $\Theta.16$ , with a 50 day lag. The poor correlation suggests active MKE conversion processes are occurring on and between the two transects. For example, an MKE peak was found at transect 4 in May 2018, when the MKE at transect 3 was only a bout 33% of it and was near a minimum during the same period. In contrast, EKE variations at transect 3 were more correlated with EKE variation at transect 4 (r=0.57 with transect 4 leading by 21 days, suggesting an upstream propagating signal of EKE between transects 3 and 4.

The barotropic conversion (BT) term stays mostly positive at transect 4 (Fig. 12c, blue line), confirming that part of the MKE is converted to local EKE, and contributes to the increase in EKE magnitude from transect 3 to transect 4. Several notable peaks of MKE→EKE barotropic conversion (BT) happened at transect 4 during May 2017, June 2017, September—October 2017, July—August 2018, and October 2018. The increases of EKE provides favorable conditions for the inverse baroclinic energy conversion (EKE→EPE) during the same periods except for July—August 2018.

During May-August 2018, monthly mean upper ocean MKE and EKE fields (Fig. 13) indicate that while the GS shifted onshore at both tran sects 3 and 4, it meandered offshore between the two transects (e.g. Fig. 13c). This offshore meander just downstream of Cape Hatteras coincided with strong EKE between 35°N and 37°N (Fig. 13g). This unique GS meandering pattern in July-August 2018 reversed the baro clinic energy conversion. Positive barotropic energy conversion (MKE →EKE) and positive baroclinic energy conversion (EKE →EPE) induced the largestEKE during the July-August 2018 at transect 4 (Fig. 12b, blue line).

At Transect 3, two strong inverse energy cascade events from EKE to MKE occurred in June 2017 and October 2018 (Fig. 12c, black line). These two inverse energy conversion events (EKE→MKE) correspond to the two largest offshore meanders of the GS in June 2017 and October 2018 near Cape Hatteras (Fig. 7b, black line).

For both transects 3 and 4, the EPE → EKE baroclinic conversions oscillated around zero (Fig. 12d). Temporal variations of BC conversion at transect 3 are smaller than at transect 4. Notably, largestbarotropic conversion (MKE→EKE) during September—October 2017 at transect 4 corresponds very well to a peak of inverse baroclinic energy conversion

(EKE→EPE) during the same period. Physically, this represents a process alternating isopycnal depths and gradients in the ocean due to eddy activity (e.g. Guo et al., 2022).

The evolution of B T and B C at transect 3 in Augus & November 2017 can be understood by examining the upper ocean monthly mean MKE and EKE fields (Fig. 14). At transect 3, the change of sign of BT energy conversion (Fig. 12c, black line) is associated with offshore meandering of the GS and am esoscale open ocean eddy that moved onshore, evolved with various eddy intensity, and ultimately dissipated into the GS (Fig. 14 upper row). This GS flow eddy interaction contributes to the local increase of MKE at transect 3 from September-October 2017 (Fig. 12a).

At transect 4, the modulation of large barotropic energy conversion (MKE → EKE) and large inverse baroclinic energy conversion (EKE → EPE) caused large fluctuations of EKE during August—November 2017. The maximum BT energy conversion and inverse BC energy conversion in September—October 2017 was also associated with GS meanders. From the time series of GS offshore distance along the Oleander line (Fig. 7a, black line), large GS offshore meanders occurred from July 2017 to August 2017, and then an onshore intrusion event occurred in September 2017.

This analysis highlights complex variations in ocean energetics modulated by GS meanders and open ocean eddies. A more general mesoscale energetics budget analysis (similar to Guo et al., 2022), needs to be pursued in a future study to better understand how ocean energetics in the mixed layer are modulated by eddy—mean flow interaction, and by diabatic mixing that is associated with a ir-sea interactions and interior diffusion.

#### 4.2. Cross stream volume, heat, and salt transport

Associated with large variations in GS kinematics and energetics are significant material transports across the mean GS path. To quantify this cross stream transport, velocity fields along the two-year mean GS path were derived from the DA model and then were rotated into the tangential (U<sub>T</sub>, positive being the GS's flowing direction) and normal (U<sub>N</sub>, positive being landward) velocity components based on the local orientation of the mean GS surface flow. The normal component of

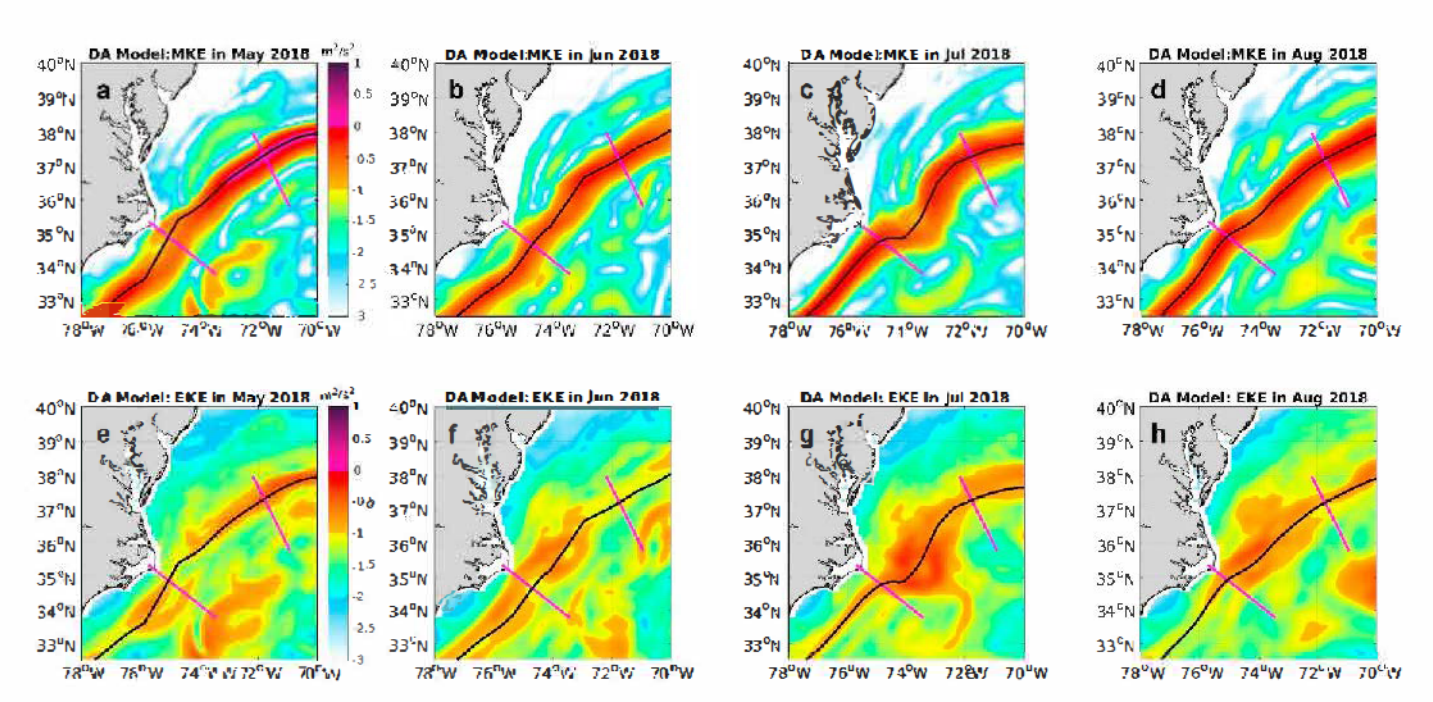


Fig. 13. Upper-ocean (integrated over the upper 200 m) monthly mean MKE (upper row) and EKE (lower row) in logg<sub>0</sub> transformed values during May (a, e), June (b, f), July (c, g) and August (d, h) 2018. Black solid lines indicate monthly mean GS paths, defined by maxim um gradient of SSH.

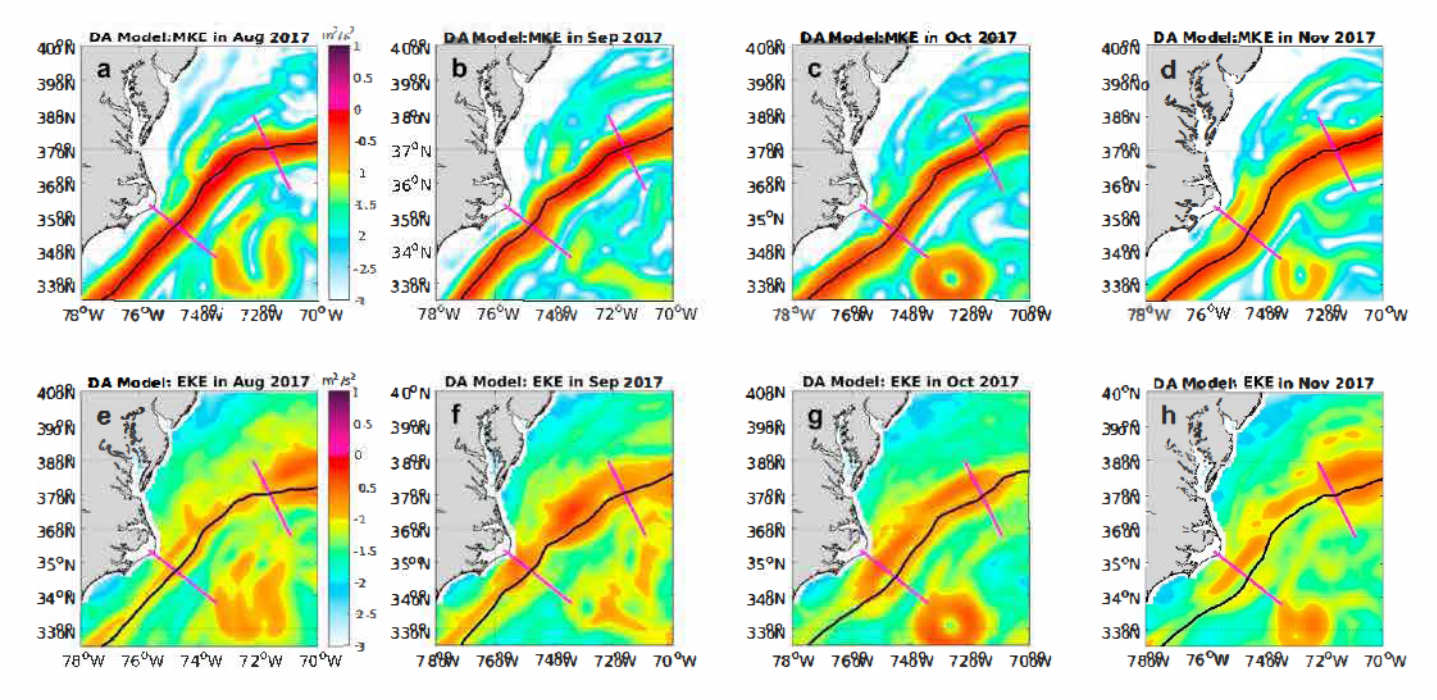


Fig. 14. Upper ocean (integrated over the upper 200 m) monthly mean MKE (upper row) and EKE (lower row) in log10 transformed values during August (a, e), September (b, f), October (c, g) and November (d, h) 2017. Black solid lines indicate monthly-mean GS paths, defined by maximum gradient of SSH.

velocity ( $U_N$ ) was integrated in depth (z) and along-stream distance (s) to yield the cross-stream upper 1000 m volume transport (Q):

$$Q = \int_{0}^{s_{o}} \int_{1000}^{\eta} u_{N}(s, \mathbf{e}) dz ds \tag{12}$$

Similarly, the cross-stream upper 1000 m eddy heat and salt transports (f) were calculated by integrating the flux  $(\emptyset)$  (Garvine et al., 1989; Gawarkiewicz et al., 2004; Chen and He, 2010):

$$f(z)e - \frac{1}{\Delta z \Delta s} \int_{z_0 - \frac{\delta z}{2}}^{z_0 + \frac{\delta z}{2}} \int_{s_0}^{s_2} \Phi(s, z') ds dz'$$
(13)

For the heat flux, Ø is defined as

$$\varnothing = \rho c_{\mathcal{P}}(T - T_n)(U_N - U_{N_m}) \tag{14}$$

For the salt flux, Ø is defined as

$$\emptyset = \frac{\rho}{1000} (S - S_{N}) (U_{N} - U_{N_{NR}})$$
(15)

where S, T,  $U_N$  and are salinity, temperature, and cross-stream normal velocity, respectively.  $\rho$  is water density and  $c_0$  is the specific heat of sea water. Subscript m denotes two-year mean values over 201 7–2018 along the selected along-stream transects.

There are two scenarios at the landward (cyclonic) side of the GS that can result in shoreward (positive) heat and salt fluxes.

- 1) GS offshore meander associated with shelf/slope water export: an offshore shift of the GS or a large shelf water export event induces transport of relatively cooler and fresher water from shelf/slope toward the GS and the open ocean. During this scenario, (Te T<sub>m</sub>), (SeS<sub>m</sub>), and (U<sub>N</sub> U<sub>Nm</sub>) are negative (U<sub>N</sub> is offshore). The resulting positive represents landward heat (salt) flux induced by the seaward transport of cooler (fresher) shelf water into the GS.
- 2) GS on shore intrusion: a shoreward shift of the GS results in  $(T T_m)$ ,  $(S S_m)$ , and  $(U_N U_{Nm})$  being positive  $(U_N)$  is on shore). The

resulting positive is generated by landward transport of warmer (saltier) GS water onto the shelf.

While both seaward transport of relatively cool and fresh shelf/slope waters and shoreward transport of relatively warm and salty GS waters result in shoreward heat and salt transports north of Cape Hatteras, these two scenarios have different physical processes and can be differentiated based on the sign of the cross-shore volume transport. As an application,

we computed the normalized cross-stream volume flux 
$$\int_{\Delta z \Delta s}^{0} \int_{R}^{s2}$$

u(s,z')dsdz, heat and salt fluxes in the GS segment between point A (intersection of transect 3 and the GS) and point B (intersection of transect 4 and the GS; see Fig. 5). Throughout the two-year time series, eddy heat and salt fluxes were predominately positive (onshore; Fig. 15 c, d). The cross-stream volume flux time series (Fig. 15 a, b) show that 56% of the time the onshore (positive) transports of heat and salt (including those peak transport events in April 2017, February 2018, and July 2018) are due to GS onshore intrusions and meanders. The remaining 44% of the time, the onshore transports of heat and salt (including those events in September 2017–January 2018, May–July 2018, and August–September 2018) are due to GS offshore meander or shelf/slope water export. The interaction between shelf circulation and the GS therefore exerted a strong influence in modulating the magnitudes of cross-stream volume, heat, and salt fluxes.

It is noted that the time series of volumee heat, and salt fluxes in Fig. 15 are 30-day low-pass filtered. They therefore represent smoothed renditions of ocean variability over the filter window. The snapshots captured on September 17, 2017 (Fig. 16a), and January 18, 2018 (Fig. 16d), serve as illustrative examples of the GS's offshore meandering during September October 2017 and its onshore intrusion during January-February 2018, respectively. On September 17, 2017, the GS shifted offshore between 35.5 and 36.5°N, causing the transport offresher shelf water (in the upper 100 m) and relatively fresh slope sea water (between 200 m and 600 m) towards the open ocean (Fig. 16b). The associated velocity anomaly for this offshore meander was negative (Fig. 16c), resulting in a significant landward cross-stream eddy salt flux indicated by the positive  $(S - S_m)(U_N - U_{Nm})$ . Similarly, on January 18,

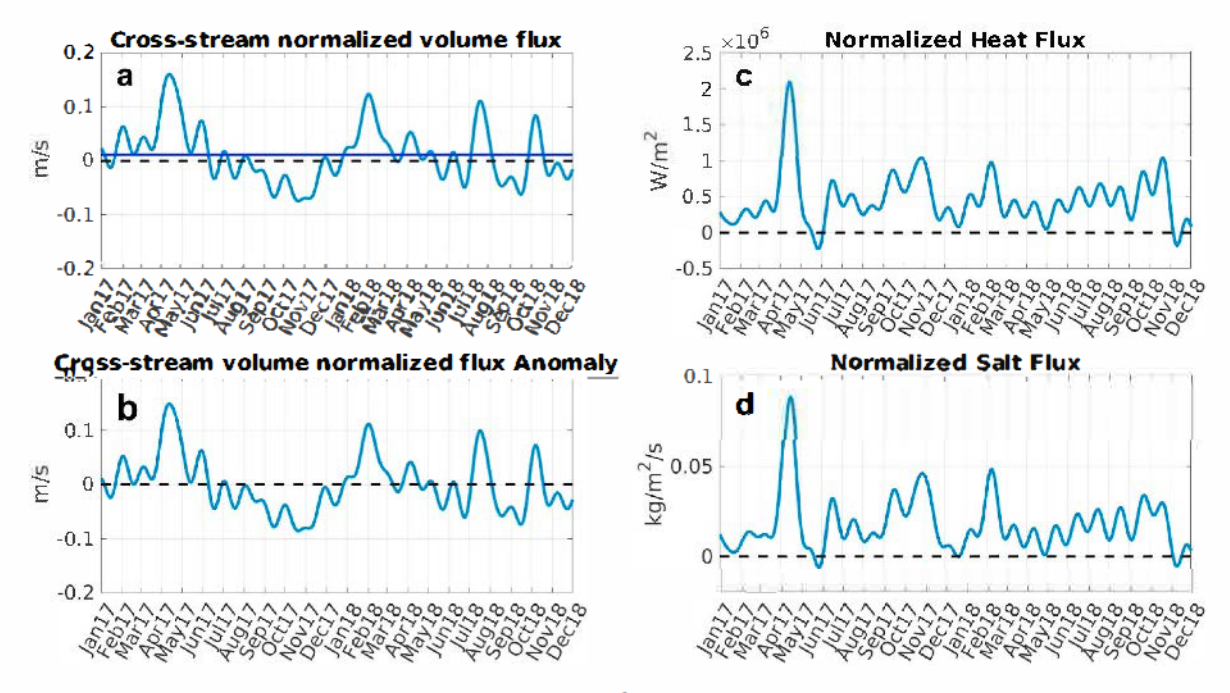


Fig. 15. Cross-stream (relative to mean GS path) a) normalized mean flux  $(\frac{1}{\Delta r \Delta s} \int_{-R}^{0} \int_{\Omega}^{2z} u(sz')ds dz)$ , b) volume flux anomaly, c) heat flux, and d) salt flux, calculated

from the DA-modeled GS between points A and B (Fig. 5). All time series are 30-day low-pass filtered. Black dashed lines denote zero value lines, blue solid lines denote two-year mean cross-stream normalized volume flux.

2018, as the GS intruded into the slope sea, its clockwise flowing circulation transported saltier GS water onshore, as shown by the positive salinity anomaly  $(S-S_m)$  in the upper 600 m starting from 200 km along the GS segment. The cross-stream normal velocity  $(U_N-U_{Nm})$  was mostly positive (Fig. 16f) between 150 km and 250 km, leading to a large landward cross-stream eddy salt flux as well. A noteworthy point worth highlighting here is that although the GS offshore meanders associated with shelf/slope water export and the GS intrusions have opposite signs in their volume fluxes, they both contribute to the onshore heat and salt transport. Together, they produce the predominately-positive (onshore) cross-stream eddy heat and salt fluxes off Cape Hatteras throughout the two-year study period.

It is noted that the volume, heat, and salt transport discussed above are defined differently from Todd (2020b)'s MAB shelf export discussion, which was based on repeated glider surveys along a shelf slope transect. In this study, we focused on the cross-stream transport, where the stream was defined by the mean GS path, as opposed to the shelf slope in the glider-based analyses. While the event-driven fresh MAB shelf water export and extremes as observed by gliders may not be fully captured by our analyses, the approach adopted can best reflect all major events associated with GS meanders. Two largest onshore volume flux were found in April 2017 and January-February 2018, respectively. In April 2017, the largest normalized heat and salt flux is associated with the largest positive (onshore) normalized cross-stream volume flux. From the time series of GS offshore distance along the transect off Cape Hatteras and along the Oleander lines, the onshore intrusions of GS occurred simultaneously along these two transects from late Match through early April 2017. During the following months from April to July 2017, the GS gradually meandered offshore along the Cape Hatteras transect and Oleanderline, thus the direction of normalized volume flux changed from onshore to offshore. The second largest positive (onshore) volume flux happened during January-February 2018. Even though the GS did not meander as much along the Cape Hatteras transect during this period, there was a 150-km shoreward shift of GS along the Oleander line, producing large onshore volume flux.

## 5. Summary and conclusions

We have developed an advanced data-assimilative (DA) ocean circulation model to investigate GS variability and its impact on cross-shelf transport during the PEACH program in 2017-2018. The modeling system uses the strong constraint 4D variational data assimilation algorithm and assimilates satellite-observed sea surface height and sea surface temperature, as well as in situ temperature and salinity profiles. The DA model reproduces the regional ocean state and GS dynamicse providing a powerful tool to fill spatial and temporal gaps in observations and to conduct circulation dynamics analysis that cannot be achieved directly from observations.

This high-resolution 4DVAR-based data-assimilative model, with a resolution of 1/15° degree, offers a more detailed representation of the Gulf Stream region compared to coarser resolution global assimilative models like ECCO (Estimating the Circulation and Climate of the Ocean) v4 and HYCOM (Hybrid Coordinate Ocean Model) global state estimate. The model employs the adjoint 4DVAR process to adjust initial conditions, allowing for the dynamic assimilation of observations and ensuring a close alignment with the real-world ocean state. This Gulf Stream data-assimilative model is particularly well-suited for studying energy conversion between mean circulation and eddy circulation, as well as heat and salt transport near Cape Hatteras. Although the ROMS 4D-Var theoretically allows for ad justment of initial condition, boundary conditions, and surface forcing, in practice, focusing solely on the initial condition as a control variable facilitates easier implementation and better interpretability of the 4DV AR system. Future advancements in data assimilation include the development of ocean-atmosphere coupled DA models and high-resolution global DA models. Coupled DA models play a crucial role in understanding and predicting climate. weather, and oceanic processes by capturing the interactions between the ocean and atmosphere. The availability of high-quality oceanic observational datasets and improved computational resources contribute to the development of more accurate and high-resolution global ocean state estimates. For instance, the Surface Water and Ocean Topography (SWOT) mission provides sea surface height

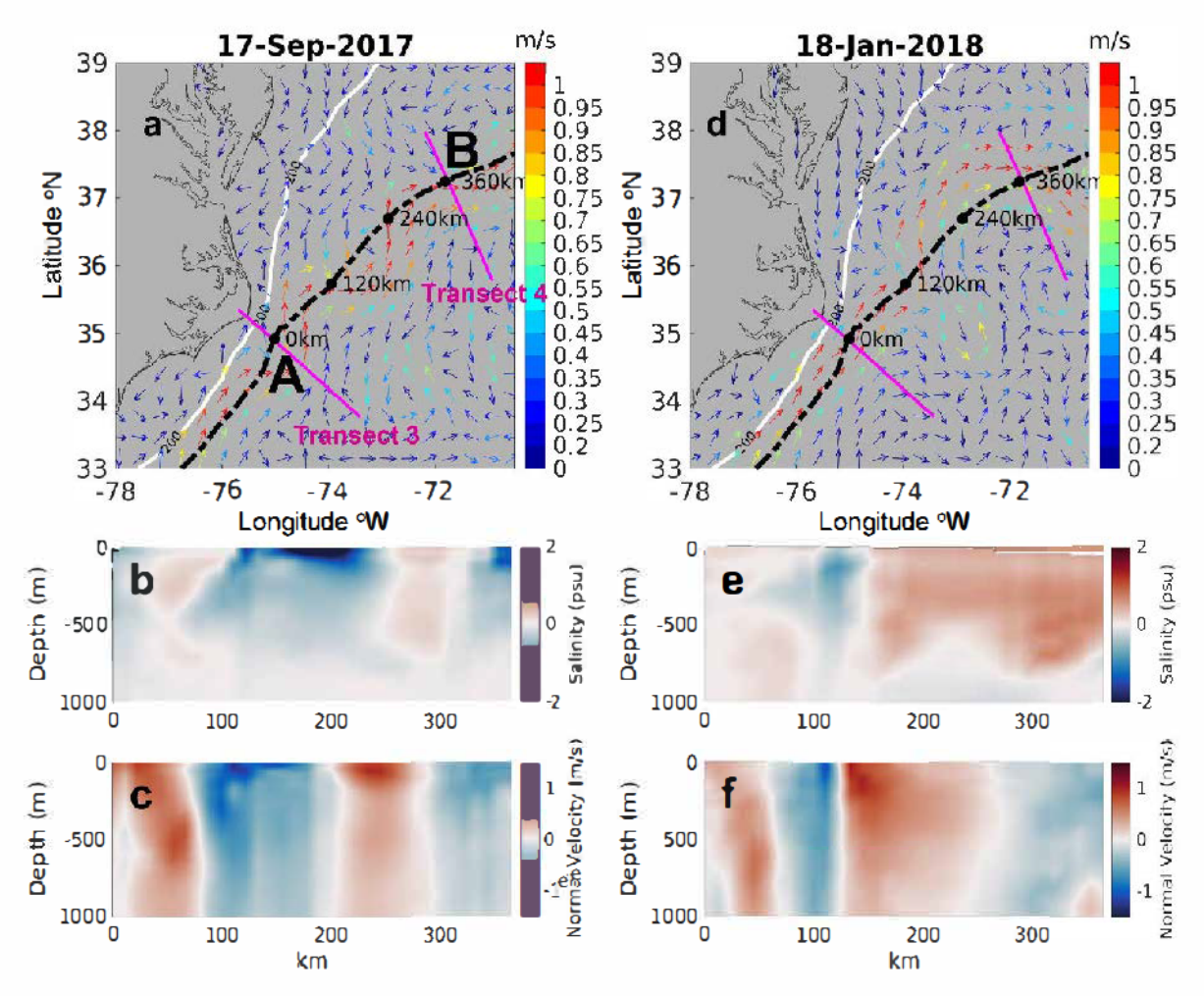


Fig. 16. Pariels (a) and (d) show the daily surface velocity fields on September 17, 2017, and January 18, 2018, respectively. The 200 m isobath is represented by white solid lines, and the two year mean Gulf Stream (GS) path is indicated by black dashed lines Transects 3 and 4 are denoted by magenta solid lines The GS segment between points A and B is used for calculating cross stream heat and salt fluxes Panels (b) and (c) present anomalies of salinity and normal velocity along the GS segment from A to B on September 17, 2017, while panels (e) and (f) show the same for January 18, 2018. Positive velocity indicates a landward direction, while negative velocity indicates a seaward direction.

measurements with a spatial resolution of approximately 1 km for the open ocean. Incorporating new types of ocean observations, such as SWOT data, is expected to enhance model representation of small-scale ocean features like eddies, currents, and coastal processes.

The goals of this study are the implementation of the dataassimilative model, model skill assessment, the mean properties of the GS and its variability near Cape Hatteras. Based on the daily 24 month DAmodel output, severalnew and expanded analyses can be pursued: 1) The GS path presents different spatial and temporal variability both upstream (Bane and Brooks, 1979; Lee et al., 1991; Gula et al., 2015) and downstream (Tracey and Watts, 1986; Savidge, 2004) of Cape Hatteras. Future studies should examine GS path variability from the Florida Current through the GS extension region. 2) Similarly, the variability of GS energetics and energy conversion need to be examined along the entire GS path. 3) How do the MAB shelf/slope sea circulation and shelf,/slope water masses affect GS onshore intrusion? During the two year study period, two large GS intrusions were identified by the onshore volume flux (Fig. 15a) in April 2017 and in January-February 2018. This is consistent with analysis of Todd (2020b), which provided glider based observational evidence of the cessation of export of MAB south of 37°N. Detailed dynamics of the shelf water and GS interaction on the synoptic time scale need to be examined in conjunction with other in situ observations.

We validated the model with standard metrics and novel higher

order metrics, including GS position and GS kinetic energy. Identification of GS position by the conventional 25 cm SSH contour approach and the maximum SSH gradient approach show consistent results along the Oleander line, but some discrepancies along transect 3 off Cape Hatteras. Caution is needed when applying different methods and data sets in identifying GS positions. The maximum SSH gradient, which identifies the core of the GS, was the approach adopted in this DA modeling study to examine the spatiotemporal variability of the GS. The GS surface MKE and EKE from three datasets (satellite altimetry, glider observations, and DA model output) were compared. The DA model and glider-based estimates agreed well. However, satellite observations under estimated the GS eddy kinetic energy, especially in the SAB. Threedimensional MKE and EKE were estimated by the model. A general consistency in subsurface MKE and EKE patterns was found between the glider observations and the DA model. The model underestimated EKE magnitude and tended to distribute energy deeper in the water column (especially at transect 4) than its observational counterpart. The discrepancy in horizontal and vertical resolution between the DA model and glider observations may have contributed to this difference.

The resulting daily ocean reanalyses were used to quantify the kinetic energy conversions and the cross stream eddy heat and salt fluxes over the two year study period. Our major findings are.

- 1) Modulations of the GS MKE and EKE were diagnosed by examining the energy conversions among MKE, EKE, and EPE through baro tropic and baroclinic conversions. Significant inverse energy cascading (EKE→MKE and EKE→EPE) occurs during GS eddy in teractions, and especially during onshore intrusions or offshore meanderings of the GS. The two largest offshore meanders of the GS near Cape Hatteras led to the two largest inverse barotropic con version events in June 2017 and October 2018.
- 2) Throughout the two-year study period, the cross stream eddy heat and salt fluxes off Cape Hatteras were predominately positive (onshore). Both the GS offshore meanders, associated with shelf/slope water export, and the GS intrusions contributed to this onshore heat and salt transport. The threelar gest onshore volume flux events induced large eddy heat and salt fluxes during April 2017 and January-February 2018, while increasing offshore volume flux from July through October 2017 was responsible for the steadily increasing eddy heat and salt fluxes during that period.

In summary, the GS has complex temporal spatial variability in its kinematics and energetics and exerts a major impact on the cross shelf transport of material properties between the continental shelf and deep ocean. Such complexity poses a significant challenge when attempting to fully capture the GS evolution and dynamics using scat tered measurements or satellite observations alone. Improved under standing and prediction of GS variability and its impact on coastal circulation require advanced observational infrastructure combining fixed, mobile, and shore-based observing components and high resolution models, together with sophisticated techniques for data assimilation. As we look for ward to our future work, the implementation of a weak constraint 4D Var approach is an important next step for addressing DA model sensitivity to boundary conditions and surface forcing as well. The development of a nested model also gains criticality as we strive for enhanced model representation of both mesoscale and submesoscale ocean processes. These advancements contribute to the dataassimilative modeling investigation of the Gulf Stream.

#### CRediT authorship contribution statement

Shun Mao: Conceptualization; Data curation; Formal analysis; Investigation; Methodology; Software; Roles/Writing original draft; Writing review & editing, Ruoying HeæConceptualization; Funding acquisition; Investigation; Methodology; Supervision; Writing review & editing, John BaneæFunding acquisition; Investigation; Writing review & editing, Glen Gawarkiewicz: Funding acquisition; Investigation; Writing review & editing, Robert E. ToddæFunding acquisition; Investigation; Methodology; Writing review & editing.

# Declaration of competing interest

The authors declare that they have no known competing financial interests or personal relationships that could have appeared to influence the work reported in this paper.

## Data availability

The Global HYCO M/NCODA product is available at https://hycom.org. Surface forcing data used in the model simulation are from the European Center for Medium Range Weather Forecast center and available online at http://apps.ecmwf.int/datasets/data/interim.full daily. Spray glider observations (Todd and Owens, 2016; Todd, 2020a) and glider based estimates of mean and eddy kinetic energy (Todd, 2021a) are available at http://spraydata.ucsd.edu. Our model assimilates: 1) level 4 sea surface height anomaly processed and distributed by the Copernicus Marine and Environment Monitoring Service https://marine.copernicus.eu/access-data; 2) Geo Polar Blended Sea Surface Temperature data developed by the NOAA

CoastWatch program and available at https://eastcoast.coastwatch.noaa.gov/cwgeopolar\_sstephp; 3) quality controlled hydrographic data processed by the UK Met Office and available at https://www.metoffice.gov.uk/hadobs/en4/en4 0 2 data sourceshtml. High resolution 4DVAR based dataassimilative model data are available at https://doi.org/10.5061/dryad.8w9ghx3rx.

#### Acknowledgments

Research support provided through NSF grant OCE 1559178, OCE 1558521 and OCE 1851421, NOAA grant NA16NOS0120028, North Carolina Renewable Ocean Energy program, and the support by the USGS/MarineHazards and Resources Program is much appreciated. We are indebted to D. Savidge, H. Seim, M. Andres, C. Edwards, and M. Muglia for valuable discussions, and to J. Warrillow for her editorial assistance.

#### References

- Andres, M., Donohue, K.A., Toole, J.M., 2020 The Gulf Stream's path and time averaged velocity structure and transport at 68.5° W and 70.3° W. Deep-Sea Res. Part I Oceanogr. Res. Pap. 156, 10.3179 https://doi.org/10.1016/j.dsr.2019.10.3179.
- Andres, M., Muglia, M., Bahr, F., Bane, J., 2018. Continuous flow of upper labrador sea water around Cape Hatteras. Sci. Rep. 8 (1), 1–8. https://doiorg/10.1038/s41598-018-22768z.
- Bane Jr., J.M., Brooks, D.A., 1979. Gulf stream meanders along the continental margin from the Floida Straits to Cape Hatteras. Geophys. Res. Lett. 6 (4), 280-282. https://doi.org/10.1029/GL006i00.4p00280.
- BaneJr., JM., Dewar, WK., 1988. Gulf stream bimodality and varia bility downstream of the Chadeston Bump. J. Geophys. Res.: Oceans 93 (GQ), 6695–6710. https://doi.org/10.1029/JC093C0Q0695.
- Baneyal M., Atkinson, L.P., Brooks, D.A., 2001. Gulf Stream physical oceanography at the Charleston Bumpodeflection, bimodality, meanders, and upwelling. In: Am. Fish. Soc. Symp. American Fisheries Society, pp. 25–36.
- Beckmann, A., Haidvogel, D.B., 1993. Numerical simulation of flowaround at all isolated seamonat. Part I: problem formulation and model accuracy. J. Phys. Oceanogr. 23 (8), 1736–1753. https://doi.org/10.1175/15200485(1993)023<173 @ NSOFAA>20 CO:2
- Bignami, F., Hopkins, T.S., 2003. Salt and heat trends in the shelf waters of the southern Middle-Atlantic Bight. Continent. Shelf Res. 23 (6), 6 42 667. https://doi.org/ 10.1016/S02.784343(03)00023-2
- Brooks, D.A., Bane, J.M., 1978. Gulf Stream deflection by a bottom feature off Chadeston, South Carolina. Science 201 (4362), 1225-1226 https://doi.org/ 10.1126/science.201.4362.1225
- Broquet, G., Edwards, C.A., Moore, A.M., Powell, B.S., Veneziani, M., Doyle, J.D., 2009. Application of 4D-variational data assimilation to the California Current system. Dynam. Atmos. Oceans 48 (1–3), 6.9-92. https://doi.org/10.1016/j dynatmore.2009.03.001.
- Chen, K., He, R., 2010. Numerical investigation of the Middle Atlantic Eight shelf break frontal circulation using a highresolution ocean hindcast model. J. Phys. Oceanogr. 40 (5), 949-964. https://doi.org/10.1175/2009JP042621.
- Chen, K., He, R., Powdl, B.S., Gawarkiewicz, G.G., Moore, A.M., Arango, H.G., 2014.

  Data assimilative modeling investigation of Gulf Stream warm core ring interaction with continental shelf and slope circulation. J. Geophys. RespOceans 119 (9), 5968-5991. https://doi.org/10.1002/2014.JC009898.
- Courtier, P., Thépant, J., Hollingsworth, A., 1994. A strategy for operational implementation of 4DV ar, using an incremental approach. Q. J. R. Meteorol. Soc. 120 (519), 13662 1387. https://doi.org/10.1002/qj.49312051912.
- Gsanady, G.T., Hamilton, P., 1988 Girculation of slopewater. Continent. Shelf Res. 8 (5-7), 565-624. https://doi.org/10.1016/0278-4343(88)900-684.
- Fairall, C.W., Bradley, E.F., Rogers, D.P., Edson, J.B., Young, G.S., 1996. Bulk parameterization of air-sea fluxes for tropical ocean global atmosphere coupledocean atmosphere response experiment. J. Geophys. Res.: Oceans 101, 3742-3764. https://doi.org/10.1029/95JG03205.
- Hagg, G.N., Schwartze, G., Gottlieb, E., Rossby, T., 1998. Operating an acoustic Doppler current profiler aboard a container vessel. J. Atmos. Ocean. Technol. 15, 2572 701. https://doi.org/10.1175/1520-04.26(1998)015<025709aadep>20.co;2.
- Hagg, C.N., Dunn, M., Wang, D., Rossby, H.T., Benway, R.L., 2006 A study of the currents of the outer shelf and upper stope from a decade of shipboard ADCP observations in the Middle Atlantic Bight. J. Geophys. Res.: Oceans 111. https://doi. org/101029/2005JC00311 6.
- Fuglister, F.C., Voorhis, AD., 1965. A new method of tracking the Gulf Stream 1. Limnol. Oceanogr. 10, R115R124 https://doi.org/10.4319/10.1965.10.suppl.2.r115
- Garvine, R.W., Wong, K., Gawarkiewicz, G.G., 1989. Quantitative properties of shelfbreak eddies. J. Geophys. Res.: Oceans 94, 14 426-1 4483. https://doi.org/ 10.1029/JG094iG10p14475.
- Gawarkiewicz, G., Brink, K.H., Bahr, F., Beardsley, R.C., Camso, M., Lynch, J.F., Chiu, C., 200 4. A large-amplitude meander of the shelfbreak front during summer south of New Englando observations from the shelfbreak PRIMER experiment. J. Geophys. Res.: Oceans 109. https://doi.org/10.1029/2002JG001468.

- Good, S.A., Martin, M.J., Rayner, N.A., 2013. EN4bquality controlled ocean temperature and salinity profiles and monthly objective analyses with uncertainty estimates. J. Geophys. Resp. Oceans 118, 6704–6716. https://doi.org/10.1002/2013JC009067.
- Gula, J., Molemaker, M.J., McWilliams, J.C., 2015. Gulf Stream dynamics along the southeastern US sea board. J. Phys. Oceanogr. 45, 690-715 https://doiorg/ 10.1175/JPO-D-14-015401.
- Guo, Y., Bishop, S., Bryan, F., Bachman, S., 2022. A global diagrosis of eddy potential energy budget in an eddy permitting ocean model. J. Phys. Oceanogr. 52, 16 6116678. https://doi.org/101126/JPO-D-22-00291.
- Haidvogd, D.B., Arango, H., Budgell, W.P., Gornnelle, B.D., Gurchitser, E., Di Lorenzo, E., Jamenlle, L., 2008. Ocean forecasting in terrain-following coordinates: formulation and skill assessment of the regional ocean modeling system. J. Comput. Phys. 227, 3595–3624. https://doi.org/10.1016/jjcp.200206.016.
- Halkin, D., Rossby, T., 1985. The structure and transport of the Gulf Stream at 73 W.

  J. Phys. Oceanogr. 15, 1439-1452. https://doi.org/10.1176/1520-0485(1985)
  0150<143935atot> 2.0.co;2:
- Han, L., Seim, H., Bane, J., Todd, R.E., Muglia, M., 2021. A shelf water cascading event near Cape Hatteras J. Phys. Oceanogr. 51, 2021-2033. https://doiorg/10.1175/ JPO-D-20-01561
- Heiderich, J., Todd, R.E., 2020. Abougstreamevolutior of Gulf Stream volume transport.
  J. Phys. Oceanogr. 50, 2251-2270. https://doi.org/10.1176/JPO-D-19-0303.1.
- Ingleby, B., Huddleston, M., 2007. Quality control of ocears temperature and salinity profiles—historical and real-time data. J. Mar. Syst. 65, 158-175. https://doi.org/ 10.1016/j.jmarsys. 2005. 11.019.
- Jouanno, J., Sheirtbaum, J., Barnier, B., Molines, J.M., Cartdela, J., 2012. Seasonal and interantual modulation of the eddy kinetic energy in the Caibbean Sea. J. Phys. Oceanogr. 42, 2041-2055. https://doi.org/10.1125/JPO-D.12048.1.
- Lee, T.N., Yoder, J.A., Atkinson, L.P., 1991. Gulf Stream frontal eddy influence on productivity of the southeast US continental shelf. J. Geophys. Res. Oceans 96, 22191-22205. https://doi.org/10.1029/91JC02450.
- Lillibridge III, JL., Mariano, A.J., 2013. A statistical analysis of Gulf Stream variability from 18 years of altimetry data. Deep Sea Res. Part II Top. Stud. Oceanogr. 85, 127-146. https://doiorg/10.1016/idsr2.2012.0703
- Manchesiello, P., McWilliams, J.C., Shehepetkin, A., 2001. Open boundary conditions for long-term integration of regional oceanic models. Ocean Model. 3, 1–20. https://doi. org/10.1016/5.1463-5003(00)00013-5.
- Masiria, S., Philarider, S., Bush, A., 1999. Ar. analysis of tropical instability waves it to rumerical model of the Pacific Oceano2. generation and energetics of the waves. J. Geophys. Res. Oceans 104, 29637-29661. https://doi.org/10.1029/ 1990.1090.2296.
- Metzger, F.J., Helber, R.W., Hogan, P.J., Posey, P.G., Thoppil, P.G., Townsend, T.L., Wall craft, A. J., Smedstad, O.M., Ratiklit, D.S., 2017. Global Oceat: Forecast System 33. Validation Test. https://doiorg/10.21236/AD103 4512. NRL Report NRL/MR/ 7320-179722
- Moore, A.M., Arango, H.G., Broquet, G., Powell, B.S., Weaver, A.T., Zavala Garay, J., 2011a. The Regional Ocean Modeling System (ROMS) 4-dimensional variational data assimilation systems: Part I-System overview and formulation. Prog. Oceanogr. 91, 34–49. https://doi.org/10.1016/j.pocean.2011.05.004.
- Moore, A.M., Arango, H.G., Broquet., G., Edwards, C., Verteziari, M., Powell, B., et al., 2011b. The regional ocean modeling system (ROMS) 4 dimensional variational data assimilation systems: Part II-performance and application to the Galifornia Current system. Prog. Oceanogr. 91, 50-73. https://doi.org/10.1016/jpocean.2011.05.003.
- Moore, A.M., Arango, H.G., Di Lorenzo, F., Miller, A.J., Cormuelle, B.D., 2009. An adjoint sensitivity arralysis of the Southern Galifornia Gurrent circulation and ecosystem.
- J. Phys. Oceatrogr. 39, 70.2720. https://doi.org/101175/2008JPO.37401.
  Olsou, D.B., Brown, O.B., Emmerson, S.R., 1983. Gulf Stream frontal statistics from Floida Straits to Cape Hatteras derived from satellite and historical data
  J. Geophys. Res. Oceans 88, 4569-4577. https://doi.org/10.1029/
  JC088 (OBp.04569.
- Pickart, R.S., Smethie Jr., W.M., 1993 How does the deep western boundary current crossthe GulfStream? J. Phys. Ocean.ogr. 23, 26022616. https://doi.org/10.1175/ 1520-0485(1993)023<26020HDTDWB> 20 GO; 2.
- Powel I, B.S., Arango, H.G., Moore, A.M., Di Lorettzo, E., Milliff, R.F., Foley, D., 2008. 4DVA Rdata assimilation in the intra-americas sea with the Regional. Ocean Modeling system (ROMS) Ocean Model. 23, 130-145. https://doi.org/10.1016/jocemod.2008.04.008

- Qiu, B., Chen, S., 2006. Decadal variability in the large-scale sea surface height field of the South Pacific Ocean coobservations and causes. J. Phys. Ocean cog. 36, 1751–1762. https://doi.org/10.1175/JPO2943.1.
- Richardson, P. L., 1983a. Eddy kinetic energy in the North Atlantic from surface drifters.

  J. Geophys. Res. Oceans 88, 4355-4369. https://doi.org/10.1029/
  JC088C0704355.
- Richardson, P.L., 1983b. A vertical section of eddy kinetic energy through the Gulf Stream system. J. Geophys. Res. Oceans 88, 2705-2709. https://doiorg/10.1029/ JC.088C04p02705.
- Rossby, T., 1987. Of the energetics of the Gulf stream at 73W. J. Mar. Res. 45, 5 9.82. https://doi.org/10.1357/00222408768400918.
- Rossby, T., Betsway, R.L., 2000. Slow variations in mean path of the Gulf stream east of Gape Hatteras. Geophys. Res. Lett. 27, 118-120. https://doi.org/10.1029/119961.0023560
- Rypina, I.I., Kamenkovich, I., Berloff, P., Pratt, I.J., 2012. Eddyir duced particle dispersion: in the meansurface North Atlantic. J. Phys. Oceanogr. 42, 2206-2228. https://doi.org/10.1126/JPO-D-11-0191.1.
- Savidge, D.K., 200 4. Gulf stream meander propagation past Cape Hatteras J. Phys. Oceanogr. 34, 2073–2085. https://doi.org/10.1175/1520.04.85(2004)034<2073:
- Savidge, D.K., Barie, J.M., 2001. Wirld and Gulf Stream influences on along-shelf transport and off-shelf export at Cape Hatteras, North Carolina. J. Geophys. Res. Oceans 106, 115 05-11527. https://doi.org/10.1029/2000JG000574.
- Savidge, D.K., Savidge, W.B., 2014. Seasonal export of South Atlantic Bightandmidatlantic Bight shelf waters at Cape Hatteras. Continent. Shelf Res. 74, 50-59. https://doi.org/10.1016/jcsr.2013.12.008.
- Seim, H.E., Savidge, D., Atidres, M., Bane, J., Edwards, C., Gawarkie wicz, G., He, R., Todd, R.E., Muglia, M., Zamboti, J., Hait, I., Mao, S., 2022. Overview of the processes driving exchange at Cape Hatteras program. Oceanography: https://doi.org/10.5670/oceanog.2022.205.
- Shchepetkin, A.F., McWilliams, J.C., 2005. The Regional Oceanic Modeling System (ROMS) to a split-explicit, free surface, topography following coordinate oceanic model. Ocean Model. 9, 348-40. https://doiogy/10.1016/pocemod.2004-08.002.
- Sikide, M.D., Janekovie, I., Kuzmie, M., 2009. A new approach to bathymetry smoothing in sigma-coordinate ocean models. Ocean Model. 29, 128-1366 https://doiorg/10.1016/pocemod@009.03.009.
- Stow, G.A., Jolliff, J., McGillicuddy Jr., D.J., Doney, S.G., Allen, J.I., Friedrichs, M.A.M., Rose, K.A., Wallhead, P., 2009. Skill assessment for coupled biological/physical models of madrie systems. J. Mar. Syst. 76, 4–15. https://doi.org/10.1016/j. imarys.2008.03.011.
- Todd, R.E., Owens, W.B., 2016 Gliders in the Gulf Stream [DataSet] Scripp's Institution of Oceanography, Institument Development Group: https://doi.org/10.21238/ SSSPRAY 2675.
- Todd, R.E., 2020a. Spray Glider Observations in Support of PEACH [Data Set]. Scripps Institution of Oceanography. Instament Development Group. https://doi.org/ 10.21238/SSSPRAY0880.
- Todd, R. E., 2020b. Export of Middle Atlantic Right shelf waters trear Cape Hatteras from two years of underwater glider observations. J. Geophys. Res. Oceans 125, e2019JC016006. https://doi.org/10.1029/2019JC016006.
- Todd, R.E., 2021a. Gulf Stream Meanand Eddy Kinetic Energy from Spray Underwater Glider Measurements [Data Set]. Scripps Institution of Oceanography, Instrument Development Group. https://doi.org/1021238/S8SPRAY2675A.
- Todd, R.E., 2021b. Gulf Stream mean and eddy kinetic energy, three-Dimensional estimates from underwater gilder observations. Geophys. Res. Lett. 48 https://doi. org/101029/2020GL090281, 2020GL090281.
- Tracey, K.L., Watts, D.R., 1986 On Gulf stream meanuler characteristics near Cape Hatteras. J. Geophys. Res. Oceans 91, 758 2-7602. https://doi.org/10.1029/ JC09iiC06ro02687.
- Warrier, J.G., Sherwood, CR., Arango, H.G., Signell, R.P., 2005. Performance of four turbulence closure models implemented using a generic length scale method. Ocean Model. 8, 81-113. https://doiorg/10.1016/jocemod.2003.12.003.
- Wood, A.M., Sheny, N.D., Huyer, A., 1996. Mixing of chlorophyll from the Middle atlantic Bight cold pool into the Gulf stream at Cape Hatteras in July 1993. J. Geophys. Res. Oceans 101, 20579-20593. https://doi.org/10.1029/96JC01135.
- Zerig, X., He, R., 2016 Gulf Stream variability and a triggering mechanism of its large meander in the South Atlantic Hight. J. Geophys. Res. Oceans 121, 8021-8038. https://doi.org/10.1002/2016JC0120720